

Proceedings

APPLIED ELECTROMAGNETICS AND MECHANICS

Edited by

Phuong Ho-Thanh, Ha Ta-Hong, Ngan Huynh-Kieu, Chi Dang-Kim

The 7th Asia Pacific Symposium on Applied Electromagnetics and Mechanics

July 25-27, 2012, Ho Chi Minh city, Vietnam



HOSEI



**KANAZAWA
UNIVERSITY**

JAPAN SOCIETY OF APPLIED ELECTROMAGNETICS AND MECHANICS

**JAPAN SOCIETY OF APPLIED ELECTROMAGNETICS AND
MECHANICS**

All rights reserved. No part of this book maybe produced, stored in a retrieval system, or transmitted, in any form or by any means without the prior written permission from the publisher.

ISBN 978-4-931455-20-7

The 7th Asia Pacific Symposium on Applied Electromagnetics and Mechanics
(2012, Ho Chi Minh city, Vietnam)

APPLIED ELECTROMAGNETICS AND MECHANICS

Proceedings of the 7th Asia Pacific Symposium on Applied Electromagnetics and Mechanics
July 25-27, 2012, Ho Chi Minh city, Vietnam

Organized by:

Faculty of Electrical and Electronics Engineering, Ho Chi Minh City University of
Technology

Editors:

Phuong Ho-Thanh, Ha Ta-Hong, Ngan Huynh-Kieu, Chi Dang-Kim

Publisher:

Japan Society of Applied Electromagnetics and Mechanics
1-4-6-401 Nezu, Bunkyo-ku, Tokyo, 113-0031 Japan

Printed in Ho Chi Minh city, Vietnam.

CONFERENCE COMMITTEE

HONORARY CHAIRMEN

Assoc.Prof. Vu Dinh Thanh	<i>Rector of Ho Chi Minh city University of Technology (HCMUT), Vietnam</i>
Prof. Junji Tani	<i>Former President of Japan Society of Applied Electromagnetics and Mechanics (JSAEM), Japan</i>
Prof. M. Enokizono	<i>President of Japan Society of Applied Electromagnetics and Mechanics (JSAEM), Oita University, Japan</i>

CHAIRMEN

Assoc. Prof. Nguyen Huu Phuc	<i>HCMUT</i>
Prof. Dang Luong Mo	<i>Advisor to VNU-HCM</i>
Prof. Yoshifuru Saito	<i>Hosei University</i>
Prof. Yasuyoshi Horibata	<i>Hosei University</i>

CO-CHAIRMEN IN ORGANIZING COMMITTEE – TECHNICAL AND PUBLICATION COMMITTEE

Prof. Yoshifuru Saito	<i>Hosei University</i>
Prof. Yasuyoshi Horibata	<i>Hosei University</i>
Prof. Hiroyuki Wakiwaka	<i>Shinshu University</i>
Dr. Do Hong Tuan	<i>HCMUT</i>
Assoc.Prof. Duong Hoai Nghia	<i>HCMUT</i>
Dr. Huynh Thai Hoang	<i>HCMUT</i>

INTERNATIONAL STEERING COMMITTEE

Chairman:

Prof. S. Yamada	<i>Kanazawa University, Japan</i>
-----------------	-----------------------------------

Co-Chairman:

Prof. A. Nafalski	<i>University of South Australia, Australia</i>
-------------------	---

Member:

M.M. Bayoumi	<i>Al-Minia University, Egypt</i>
S. Chonan	<i>Akita Prefectural University, Japan</i>
K. Demachi	<i>University of Tokyo, Japan</i>
Prof. J. Faiz	<i>University of Tehran, Iran</i>
E. Okada	<i>Ibaraki University, Japan</i>
Y. Saito	<i>Hosei University, Japan</i>
M. Sasaki	<i>Gifu University, Japan</i>
N. Takahashi	<i>Okayama University, Japan</i>
R. Tang	<i>Shenyang University of Technology, China</i>
M. Uesaka	<i>University of Tokyo, Japan</i>
H. Wakiwaka	<i>Shinshu University, Japan</i>
C. Xiang	<i>North China Electrical Power University</i>
M. Yamamoto	<i>The University of Tokyo, Japan</i>
W.L. Yan	<i>Hebei University of Technology, China</i>
M. Norhisam	<i>Universiti Putra Malaysia, Malaysia</i>
J.G. Zhu	<i>UTS, Australia</i>
K. Chamnongthai	<i>KMUTT, Thailand</i>
Anuar Mohd Ramli	<i>Telekom Malaysia Berhad</i>
T. Ohji	<i>Toyama University, Japan</i>

H. Okazaki
T. Yuji

*Gifu University, Japan
University of Miyazaki, Japan*

ORGANIZING COMMITTEE

Chairman:

Dr. Norhisam Misron

UPM, Malaysia

Co-Chairman:

Dr. Ismail Musirin

UiTM, Malaysia

Members:

Wan Zuha Wan Hassan

UPM, Malaysia

Assoc. Prof. Dr. Mohammad Hamiruce Marhaban

UPM, Malaysia

Dr. Mohd Nizar Hamidon

UPM, Malaysia

PUBLICATION COMMITTEE

Chairman:

T. Sawada

Keio University, Japan

Co-Chairman:

Roslina Mohd Sidek

UPM, Malaysia

H. Ohsaki

University of Tokyo, Japan

CONTRIBUTORS

Japan Society of Applied Electromagnetics and Mechanics

Ho Chi Minh City University of Technology, Vietnam

Hosei University, Japan

Kanazawa University, Japan

Transformers for Contactless Power Suppliers

Tatsuya OHASHI¹⁾, Iliana MARINOVA²⁾ and Yoshifuru SAITO¹⁾

¹⁾ Graduate School of Hosei University, Tokyo 184-8584, Japan

²⁾ Technical University of Sofia, Sofia 1756, Bulgaria

ABSTRACT

Contactless power supplier is composed of a transformer having the distinct primary and secondary coils separated by air gap. Because of the electromagnetic compatibility problem, it is essential to keep the leakage magnetic fields around the contactless power supplier as low as possible.

This paper carries out the wavelets multi-resolution analysis to the magnetic field distributions around contactless power supplier. As a result, we have succeeded in obtaining one of the reasonable core shapes by observing the wavelets spectra of measured magnetic field vector distributions. Furthermore, it is revealed that a tested trial transformer gives nearly 80 percent power transmission efficiency even though the primary and secondary coils are separated by 10mm air gap.

Keywords: contactless power suppliers, magnetic field visualization, discrete wavelets, multi-resolution analysis.

1 Introduction

Development of modern semiconductor technology makes it possible to realize small and light weight electronic devices equipped with a large variety of smart functions such as smart cellular phone as well as ultra mobile computers.

Although these electronics provide the highly efficient job environment, entertainments and convenient electronic consumer life, environments around human life are filling up with the electromagnetic fields. Particularly, because of the many electric power suppliers to supply the electronic products, it is essentially accompanied the electric power lines jangle, which leads to SAR (specific absorption rate) problems.

One of the solutions of this electromagnetic compatibility problem in the human life environment is to work out the cordless contactless power suppliers [1].

This paper concerns with development of a transformer composed of the separated primary and secondary cores by air gap. This transformer having the open magnetic flux paths between the primary and secondary core is of the paramount part to realize the contact-less power suppliers.

Apply the discrete wavelets transform to the magnetic field vector distributions around the transformer having open magnetic flux paths clarifies that the dish like ferrite cores embedding spirally wound coils gives a far excellent magnetic field vector distribution compared with those with

conventional U shape cores [2,3]. An extension of conventional inner core type transformer employing U shape cores spreads the magnetic fields around the transformer centered at the air gaps. On the other side, a flat transformer employing dish shape ferrite cores and spirally wound coils (called the "flat transformer" in short) confines the magnetic fields at the center of the flat transformer, which minimizes the magnetic fields around the transformer.

As a first stage, we have worked out the trial flat transformers. Experimental study utilizing secondary resonant technique reveals that our flat transformer with 1cm air gap and 0.69 coupling factor is capable to transmit 79 percent input power to the secondary circuits [4]. Further, multi-resolution analysis of the discrete wavelets clarifies the effect of secondary resonance circuits, i.e., the highest level the magnetic field vector distributions visualizes the distinct difference of the magnetic field vector distributions between the secondary resonant and not resonant conditions.

2 Visualization of the Magnetic Field Around the Transformers

2.1 Transformer employing U shape ferrite core

Fig.1 shows the tested transformer employing two U shape ferrite cores. Table 1 lists specification of this transformer.

We have carried out the measurements of magnetic field vector distributions around this transformer using a search

coil. The shape of this coil is a finite length solenoid and dimensions are the 1cm length, 14mm diameter, 30 turn wound coil using a 0.2mm diameter conducting wire. By means of this search coil, we have measured the magnetic field vector distributions.

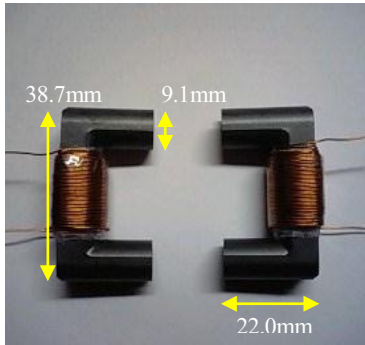


Fig.1 Tested transformer employing U shape ferrite cores.

Table 1 Specification of the transformer employing U shape cores.

U shape core	TDKPE22UU
Number of turns of primary coil	30turns
Number of turns of secondary coil	30turns
Diameter of primary coil	0.4mm
Diameter of secondary coil	0.4mm

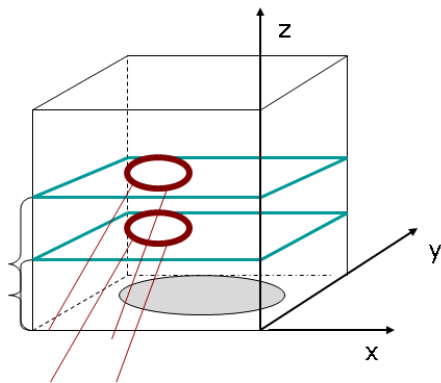


Fig.2 Scheme for measurement of the magnetic field vector distribution.

Fig. 2 shows a scheme for measurement of the magnetic field vector distribution. In this figure, the circular coils are the search coils. Two parallel surfaces illustrate the magnetic field measurement surfaces in the direction of z-axis component. Number of measured points is $8 \times 8 \times 4$ with respect to the x-, y-, z-directions. Secondary circuit is no load and primary is excited by a 10kHz sinusoidal 0.5A

current. The air gap between the heads of both primary and secondary U shape ferrite cores is of 1 cm.

Fig.3 shows one of the measured magnetic field vector distributions at some instance. It is obvious that the magnetic field vectors distribute around the U shape cores.

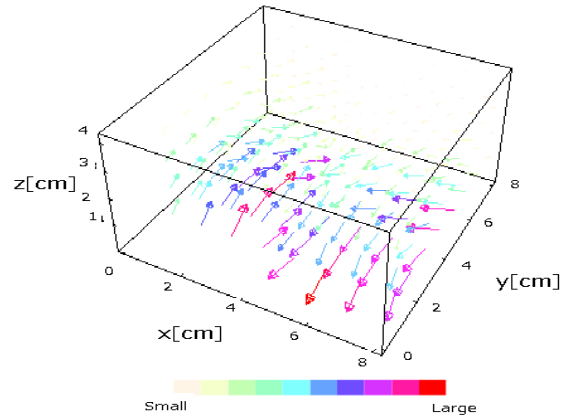


Fig.3 Magnetic field vector distribution around the transformer employing U shape ferrite cores.

2.2 Flat Transformer

The transformer employing U shape cores is essentially one of the extensions of in-core type transformer. On the other side, the flat transformer is one of the extensions of shell type transformer. Fig. 4 shows the tested flat transformer employing dish like ferrite cores. The dish like



Fig. 4 Tested transformer employing the dish like ferrite cores.

ferrite cores are composed of the Manganese and Zinc compound, and their customized products have been worked out by Tokin company.

Experimental measurement of the magnetic field vector distributions is carried out by means of the same search coil used to the transformer employing the U shape ferrite cores.

Fig.5 shows a scheme of the magnetic field vector

distribution measurements for this flat transformer. In this figure, the primary and secondary coils are spirally wound. Two parallel square surfaces illustrates the magnetic field measurement locations in the direction of z-axis component. Number of measured points is $8 \times 8 \times 4$ with respect to the x-, y-, z-directions. The secondary circuit is no load and the primary circuit is excited by a 10kHz sinusoidal 0.5A current. The air gap between the primary and secondary core head surfaces is of 4 cm.

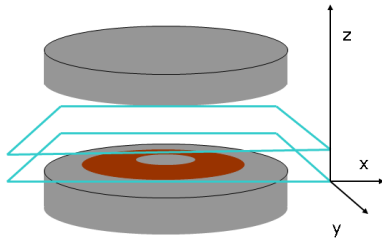


Fig.5 Scheme for measurement of the magnetic field vector distribution for the flat shape transformer.

Table 2 lists specification of the flat shape transformer shown in Figs. 4 and 5.

Table 2 Specification of the flat shape transformer.

Primary core: Outer diameter	105mm
Primary core: inner diameter	99 mm
Primary core: thickness	7mm
Primary core: diameter	105mm
Primary core: depth of the cylinder cut	1mm
Primary core: length of the spiral winding	506.3mm
Primary core: diameter of the conductor	4mm
Secondary core: Outer diameter	105mm
Secondary core: inner diameter	99mm
Secondary core: thickness	7mm
Secondary core: diameter	105mm
Secondary core: depth of the cylinder cut	1mm
Secondary core: length of the spiral winding	506.3mm
Primary core: diameter of the conductor	4mm

Fig.6 shows one of the measured magnetic field vector distributions at some instance. It is obvious that the magnetic field vectors spreads over primary winding like a fountain, and also it is revealed that nature of the magnetic field distributions is intrinsically different between the in-core type in Fig.3 and shell- core type in Fig.6 .

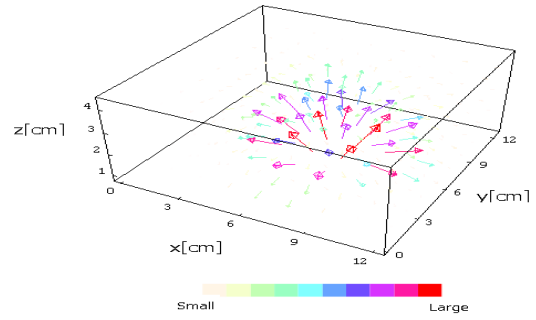


Fig.6 Magnetic field vector distribution between the flat shape cores.

3 The Wavelets Transform Analysis

3.1 Vector Wavelets Transform

The magnetic field vector distributions are generally three dimensional vectors. Therefore, when we apply the wavelets multi-resolution analysis to the three dimensional vectors, it leads to the three-dimensional vector wavelets transform [2,3].

When we denote a transpose operation of a three-dimensional (cubic) matrix A_{lmn} as

$$[A_{lmn}]^T = A_{mnl} \quad , \quad (1)$$

the three-dimensional wavelets spectrum matrix S_{lmn} is given by

$$S_{lmn} = \left[W_n \cdot \left[W_m \cdot \left[W_l \cdot A_{lmn} \right]^T \right]^T \right]^T \quad . \quad (2)$$

where the matrix S_{lmn} is a three-dimensional wavelets spectrum matrix with order l by m by n ; and W_n , W_m and W_l are the wavelets transform matrix with order n by n , m by m and l by l , respectively.

The measured magnetic field vectors distribute in three-dimensionally so that the magnetic field vector distribution matrix \mathbf{H}_{lmn} is composed of the three independent x-, y-, and z-vector component matrices \mathbf{X}_{lmn} , \mathbf{Y}_{lmn} , \mathbf{Z}_{lmn} , respectively.

The matrix \mathbf{H}_{lmn} is represented by

$$\mathbf{H}_{lmn} = \mathbf{X}_{lmn} + \mathbf{Y}_{lmn} + \mathbf{Z}_{lmn} \quad . \quad (3)$$

Thus, the three-dimensional wavelets spectra of the magnetic field distribution are obtained by

$$\mathbf{S}_{lmn} = \left[W_n \cdot \left[W_m \cdot \left[W_l \cdot (\mathbf{X}_{lmn} + \mathbf{Y}_{lmn} + \mathbf{Z}_{lmn}) \right]^T \right]^T \right]^T \cdot (4).$$

Generally, the wavelets spectrum \mathbf{S}_{lmn} is classified into the multi-level spectra according to the orthogonal property of discrete wavelets transform. Number of levels p depends on not only the number of data comprising spectrum \mathbf{S}_{lmn} but also the wavelets base functions used for wavelets transform matrices W_n, W_m, W_l .

Apply the inverse wavelets transform to each of the decomposed wavelets spectra $\mathbf{S}_{lmn}^{(1)}, \mathbf{S}_{lmn}^{(2)}, \dots, \mathbf{S}_{lmn}^{(p)}$ yields the wavelets multi-resolution result:

$$\begin{aligned} \mathbf{H}_{lmn} &= \sum_{i=1}^p \mathbf{H}_{lmn}^{(i)} \\ &= \sum_{i=1}^p \left[W_n^T \cdot \left[W_m^T \cdot \left[W_l^T \cdot \mathbf{S}_{lmn}^{(i)} \right]^T \right]^T \right]^T, \end{aligned} \quad (5)$$

where the levels 1,2, .. . p-th magnetic field vector distributions are $\mathbf{H}_{lmn}^{(1)}, \mathbf{H}_{lmn}^{(2)}, \dots, \mathbf{H}_{lmn}^{(p)}$, respectively. Low and higher level magnetic field vector distributions represent the global and precise vector distributions, respectively. Sum of the entire levels gives the original vector field distribution.

3.2 Wavelets analysis of the magnetic field vector distribution around the transformer employing U shape ferrite cores

Fig.7 shows the wavelets spectra of the magnetic field vector distribution shown in Fig.3, where Daubechies second order base function is employed. It must be noted that wavelets transform to the vector fields gives the vector fields even in the wavelets spectrum space. Further, the most dominant wavelets spectrum vectors are extracted as observed in Fig. 7.

Because of the number of data in z-axis and also employed Daubechies second order base function, it is possible to obtain the three levels multi-resolution magnetic field vector distributions. These magnetic field vector distributions are shown in Fig. 8.

The results of the wavelets multi-resolution analysis to the transformer employing U shape cores suggests that major magnetic flux linking both of the primary and secondary cores is only the level 1 magnetic field vectors.

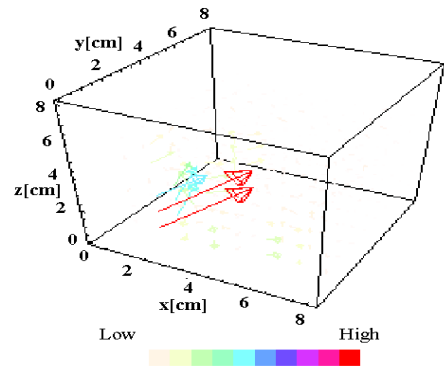
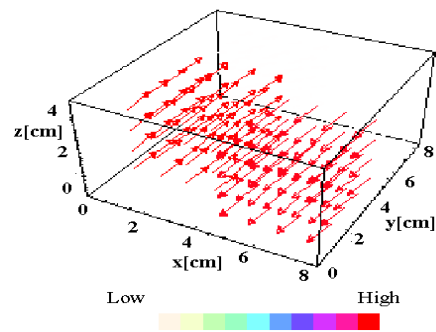
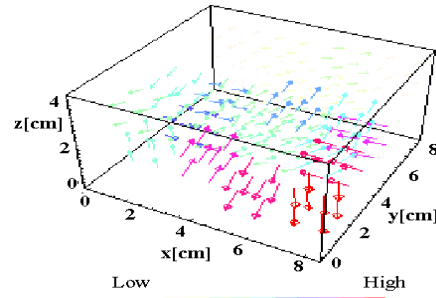


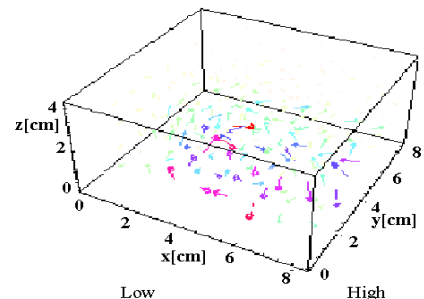
Fig.7 Wavelets spectra of the magnetic field vector distribution measured around the transformer employing U shape cores..



(a) Level p=1



(b) Level p=2



(c) Level p=3

Fig.8 Wavelets multi-resolution analysis results of the magnetic field vector distribution measured around the transformer employing U shape cores.

This means that the levels 2 and 3 magnetic fields vectors are spreading around cores centering the air gap. This spreading magnetic field vector distribution causes the electromagnetic compatibility problem.

3.3 Wavelets analysis of the magnetic field vector distribution around the flat transformer

Fig.9 shows the wavelets spectra of the magnetic field vectors distribution shown in Fig.6, where Daubechies second order base function is employed. The most dominant wavelets spectrum vectors are extracted as observed in Fig. 9.

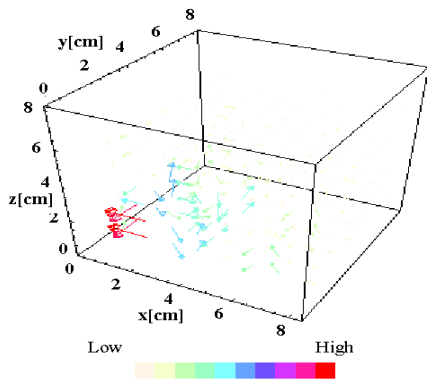


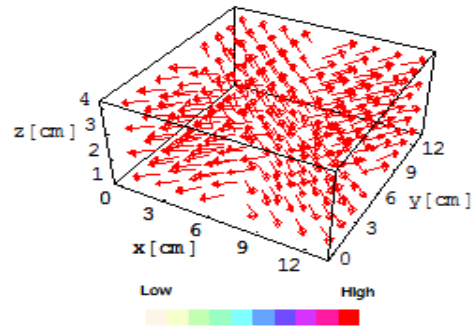
Fig.9 Wavelets spectra of the magnetic field vector distribution measured around the flat transformer.

Because of just the same reason as described in section 3.2, number of data in z-axis and also employed Daubechies second order base function, it is possible to obtain the three levels multi-resolution magnetic field vector distributions.

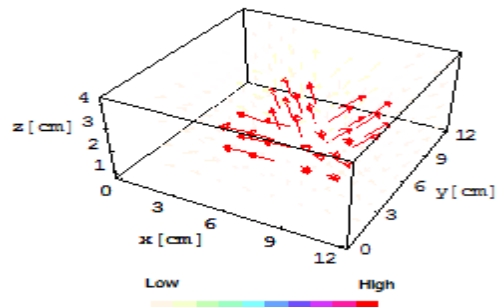
Fig. 10 shows the magnetic field vector distributions in each level.

The results of the wavelets multi-resolution analysis to the flat transformer suggest that major magnetic fluxes linking both of the primary and secondary cores are the levels 1 and 2 magnetic field vectors. Even though the level 3 magnetic field vectors starts from primary core and return to the same primary core, it is possible to reveal that they are regularly distributing along with the surface of primal core as well as coil.

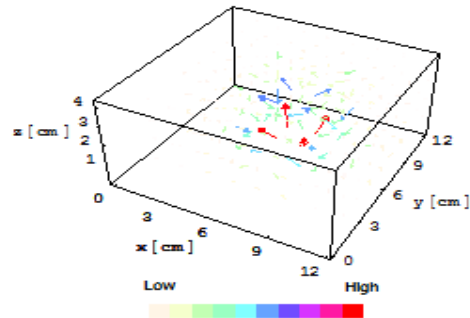
This means that the flat transformer minimizes the leakage magnetic fields from the air gap space between the primary and secondary core surfaces.



(a) Level p=1



(b) Level p=2



(c) Level p=3

Fig.10 Wavelets multi-resolution analysis results of the magnetic field vector distribution measured around air-gap of the flat transformer.

Thus, the flat transformer has far excellent magnetic field vector distribution characteristic from the viewpoint of the electromagnetic compatibility.

4 Fundamental Characteristics of the Flat Transformer

4.1 Coupling factor

A coupling factor κ is one of the most important transformer characteristics, which indicates smallness of the leakage magnetic field vectors between the primary and

secondary coils. Namely, as possible as large coupling factor κ means as possible as small magnetic field vector distribution around the transformer.

Let us consider a simplified circuit model of the transformer shown in Fig. 11 to evaluate the coupling factor κ . The dots '•' shown over the primary and secondary coils in Fig. 11 show the positive induced voltages at each of the coil terminals.

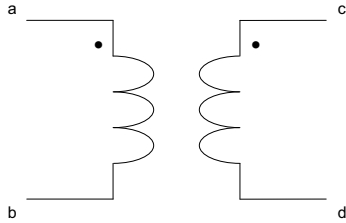


Fig.11 Simplified circuit model of transformer to evaluate the coupling factor κ .

When we connect each of the terminals in Fig. 11 to additive polarity as shown in Fig. 12(a), it is possible to obtain the following relationship:

$$L_a = L_1 + L_2 + 2M, \tag{6}$$

where L_a , L_1 , L_2 and M are the additive-, primary self-, secondary self- and mutual inductance, respectively.

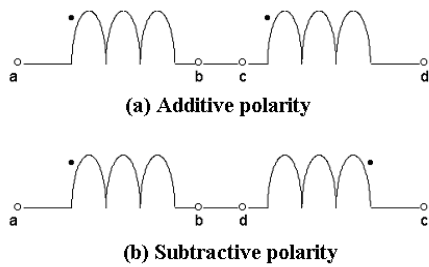


Fig.12 Series connection of the primary and secondary coils shown in Fig. 11.

Also, when we connects each of the terminals in Fig. 11 to subtractive polarity as shown in Fig. 12(b), we have

$$L_s = L_1 + L_2 - 2M, \tag{7}$$

where L_s is a subtractive-inductance.

Further, the primary and secondary self inductances can be measured independently. Thereby, combination of (6) and (7) leads to the mutual inductance M and coupling factor,

which are respectively given by the following equations

$$M = \frac{L_a - L_s}{4}, \tag{8}$$

$$k = \frac{M}{\sqrt{L_1 L_2}}.$$

Table 3 shows the measured inductances L_a , L_s , L_1 , L_2 and coupling factor κ changing the air-gap length between the primary and secondary core surfaces.

Table 3 Coupling factor of the transformer employing flat shape cores measured at 30kHz.

Gap[mm]	0	1	3	5	7	10
$L_1[\mu\text{H}]$	578.6	348.2	231.1	181.6	169.9	133.9
$L_2[\mu\text{H}]$	572.7	348.1	229.4	181.0	168.3	133.3
$L_s[\mu\text{H}]$	2297.4	1358.2	881.8	669.4	617.6	450.8
$L_a[\mu\text{H}]$	16.9	26.1	41.4	56.0	61.1	84.3
κ	0.99	0.96	0.91	0.84	0.82	0.69

The results listed in Table 3 suggests that the flat transformer is capable of keeping the good coupling factors $\kappa \approx 0.7$ although the primary and secondary coils are separated by air-gap of 1cm.

4.2 Power transmission rate

Power transmission rate is the other important characteristic, which indicates the efficiency of the transformer.

To improve the transformer efficiency, a secondary resonance between the capacitor and secondary leakage inductance is widely used and well known technique [4].

Fig. 13 shows a simplified circuit model attaching a resonant capacitor C .

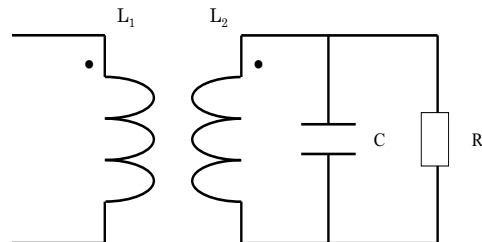


Fig. 13 Circuit diagram of a secondary resonant type transformer.

Attaching 40 μF resonant capacitor in parallel to the

secondary coil terminal of the flat transformer leads to a nearly $\varepsilon \approx 80\%$ input power transmission rate defined by

$$\varepsilon = \frac{\text{Secondary output power}}{\text{Primary input power}} \times 100[\%]. \quad (9)$$

4.3 Multi-resolution analysis of the flat transformer under load condition

As described in Section 3.2, we have described about the magnetic field vector distribution and its wavelets multi-resolution analysis results. To demonstrate the usefulness of the flat transformer, it must be demonstrated that the transformer under loaded condition never stimulate the magnetic field vectors around the transformer centered at air gap.

Fig. 14 shows a measured magnetic field vector distribution at some instance of the flat transformer under the 1Ω pure resistive load and secondary resonant conditions. Measurement conditions and method of the magnetic field vectors is just the same as that of Section 2.2.

Observe the magnetic field vector distribution in Fig. 14 reveals that the flat transformer under the loaded condition reduces the entire magnetic field vectors due to the secondary load current.

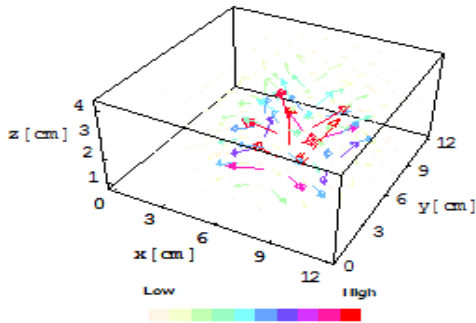
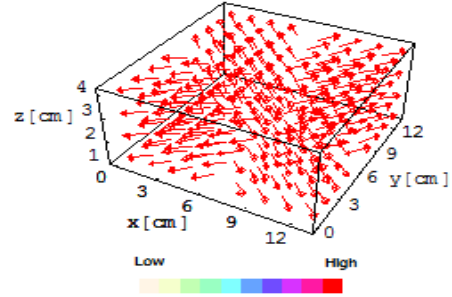


Fig.14 Magnetic field vector distribution of the flat transformer under the 1Ω pure resistive load and secondary resonant conditions.

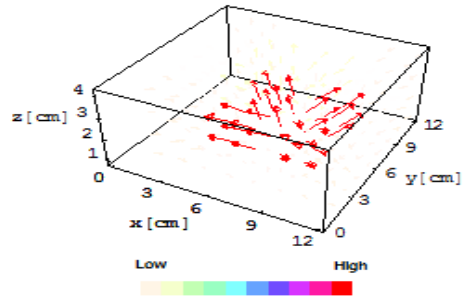
Further, a discrete wavelets multi-resolution analysis to this magnetic field vector distribution shown in Fig. 15 reveals that the magnetic field vectors at level $p=3$ focus on the center of spirally wound primary coil. This means that the leakage magnetic flux is dramatically reduced compared with those of under no load condition shown in Fig. 10(c).

Also, comparison the wavelets multi-resolution results shown in Fig. 11 with that of Fig. 15 suggests that the level

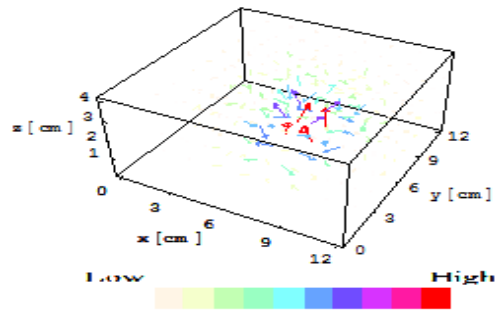
$p=2$ as well as level $p=3$ demonstrate the dramatic reducing of the magnetic field vectors spreading to the outside direction from the center of both primary and secondary coils.



(a) Level $p=1$



(b) Level $p=2$



(c) Level $p=3$

Fig.15 Results of the wavelets multi-resolution analysis to the flat transformer under the 1Ω pure resistive load and secondary resonant conditions.

To check the secondary resonance circuit effect, we have carried out the discrete wavelets multi-resolution analysis to the magnetic field vector distribution of flat transformer under the 1Ω pure resistive load and secondary non-resonant conditions.

Fig.16 show a level $p=3$ magnetic field vector distribution of the wavelets multi-resolution analysis results.

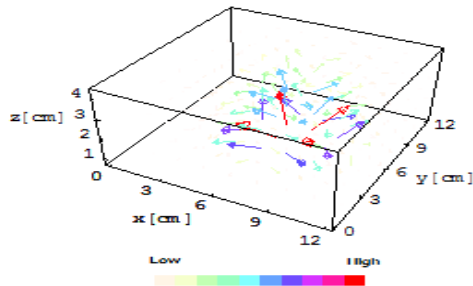


Fig.16 Level $p=3$ magnetic field vector distribution of the flat transformer under the 1Ω pure resistive load and secondary non resonant conditions.

One of the big differences between the level $p=3$ field vector distributions shown in the Figs. 15(c) and 16 is that the most dominant vectors located at the center take the opposite directions. Namely, the dominant vectors in Fig. 15(c) direct toward the center but that of Fig. 16 direct toward the outward from the center. Thus, it is clarified that the resonance of secondary circuit increases the linkage flux to the secondary coils. This leads to a highly efficient power transmission rate.

5 Conclusion

To develop the contactless power suppliers, this paper has worked out one of the reasonable transformers having open magnetic flux path.

The reasons why the flat transformer is one of the most reasonable transformers are as follows.

At first, our proposed transformer suppresses the leakage magnetic fields around the core, because it is a natural extension of the shell type core structure.

Second, by means of the multi-resolution analysis of the discrete wavelets, the primary and secondary coils would spirally focus on the magnetic field vectors to the center of both primary and secondary coils. Finally, even though the air gap is relatively large and small coupling factor, it is possible to transmit the electrical power from the primary to the secondary circuits with relatively high efficiency.

One of the drawbacks of the exploited transformer is a weight compared with those of core type transformer.

References

- [1] S.Takada, Y.Saito and K.Horii, Visualization of the magnetic field vectors around the contact-less power suppliers, Japan Society of Visualization, Proceedings of the Visualization Symposium in 2000, Paper No. P01-001.
- [2] S.Matsuyama, S.Matsuyama, Y.Saito, Data Handling Methodology for Discrete Wavelets and Its Application to The Dynamic Vector Fields, International Journal of Wavelets, Multiresolution and Information Processing, Vol.4, No.2, June (2006) pp.263-271. World Scientific Publishing Company.
- [3] S.Matsuyama, Y.Oguchi, Y.Saito, T.L.Kunii, Handling Technique of the Dynamic Color Computer Graphics by the Wavelets transform, Japan Society of Visualization, Proceedings of the Visualization Symposium in 1999, Paper No. 206.
- [4] Harrison, J.L., A new resonance transformer, Electron Devices, IEEE Transactions on Issue Date: Oct 1979 Vol.26 Issue: 10, pp. 1545 - 1

Enhance the Sensibility of the Eddy Current Testing

Hiroki KIKUCHIHARA¹, Iliana MARINOVA², Yoshifuru SAITO¹,
Manabu OHUCH³, Hideo MOGI³ and Yoshiro OIKAWA³

¹ Graduate School of Hosei University, Tokyo 184-8584, Japan

² Technical University of Sofia, Sofia 1756, Bulgaria

³ Denshijiki Industry Co., Ltd, Tokyo 115-0051, Japan

Eddy current testing (ECT) is one of the most representative nondestructive testing methods for metallic materials, parts, structures and so on. Operating principle of ECT is based on the two major properties of magnetic field. One is that alternating magnetic field induces eddy current in all of the conducting materials. Thereby, an input impedance of the magnetic field source, i.e., electric source, depends on the eddy current path. Second is that the magnetic field distribution depends only on the exciting but also the reactive magnetic fields caused by the eddy currents in targets. Former and latter are the impedance sensing and magnetic flux sensing types, respectively.

This paper concerns with an improvement of sensibility of the impedance sensing method. Sensibility of the ECT is improved by means of two steps. One is an optimum exciting frequency selection. We employ the natural parallel resonant frequency of ECT coil. The other is to increase the sharpness of the resonance curve on impedance versus frequency characteristic by changing the coil connection. Thus, we have succeeded in developing the ECT sensor having up to 4 times higher sensibility compared with those of conventional one.

Key words: Eddy current, Nondestructive testing, Resonant frequency

1 Introduction

Modern engineering products such as air-plane, automobile, smart building, high speed train and so on are essentially composed of metallic materials for forming the shape of product, suspending the mechanical stress and constructing the structural frames. In particular, the mass transportation vehicles, e.g. large air plane, hi-speed train, express highway bus and so on, carrying a large number of people are required ultimately high safety as well as reliability.

To keep the safety of such vehicles, nondestructive testing to the metallic materials is one of the most important technologies because most of the structure materials are composed of the metallic materials.

Various nondestructive testing methods, such as eddy current testing (ECT), electric potential method, ultrasonic imaging and x-ray tomography, are currently used. Among these methods, ECT does not require complex electronic circuits and direct contact to target. Furthermore, target whose major frame parts are composed of conductive metallic materials can be selectively inspected by ECT [1,3].

Operating principle of ECT is very simple. The ECT is based on the two major properties of magnetic field. One is that exposing the conductive materials to the alternating

magnetic fields induces eddy current in all of the conducting materials. Thereby, the input impedance of the magnetic field source, i.e., electric source, can detect the change of the target impedance caused by defects blocking eddy current flowing. The ECT based on this principle is called impedance sensing type. The other type utilizes a separately installed sensor coil to detect the leakage magnetic flux change. The magnetic field of ECT is composed of two components: one is the exciting and the other is the reactive magnetic fields. The reactive magnetic field is caused by the eddy currents in the target so that change of eddy current paths changes the reactive magnetic fields. Thus, the independently installed sensor detects this magnetic field change. This type is called a separately sensing coil type.

This paper concerns with an improvement of sensibility of the impedance sensing method. Improvement of the sensibility is carried out in the two major steps.

The first step is to select the optimum exciting frequency. We select the natural parallel resonant frequency of the ECT sensor coil when facing with a wholesome part of target. A system comprising the ECT facing with the wholesome part of target takes the maximum pure resistive impedance. When the ECT sensor coil meets with a defect of target, this resonance condition is essentially not satisfied. This makes it possible to maximize the deviation between the resonance and not resonance impedances.

The second step is to increase the resonant impedance as well as to sharpen the peaky impedance versus frequency characteristic by changing the coil connection [4]. Since the natural parallel resonance impedance become larger, then the deviation between the resonance and not resonance impedances is essentially larger. This essentially enhances the sensibility of ECT sensor.

2 Enhancement of ECT Sensibility

2.1 Operating principle of ECT

Let an arbitrary finite length solenoid coil shown in Fig. 1(a) be an eddy current sensor coil. When we put on this sensor coil on a copper plate as shown in Fig. 1(b) and apply an alternating current to the sensor coil, because of the Faraday's law, eddy current is induced as a reaction of the alternating magnetic fields. Measure the input impedance of the sensor coil is able to diagnose a difference of the target copper plate condition between no defects (Fig. 1(b)) and 2mm crack defect(Fig. 1(c)). This is similar to the secondary impedance change detection from primary input terminal in a conventional single phase transformer.

Thus, it is obvious that a simple finite length solenoid coil can detect the defects of the target conducting materials. This is the operating principle of ECT.

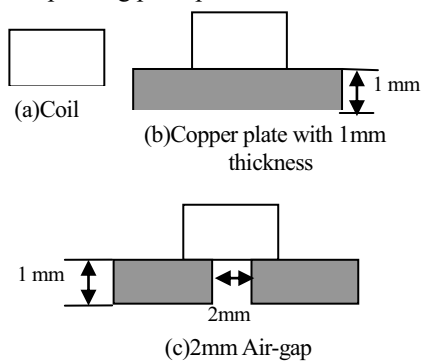
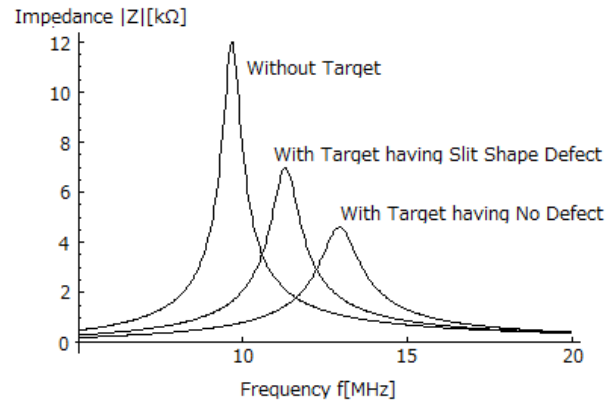


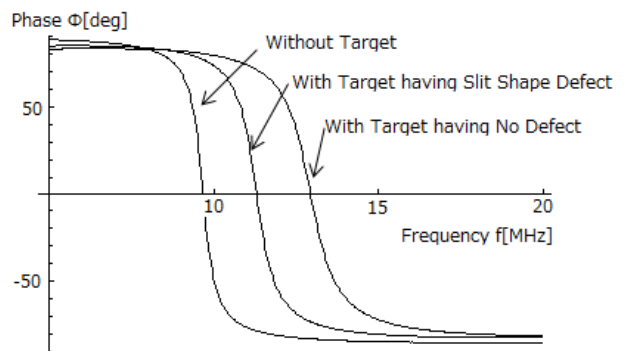
Fig.1 Tested coil and the measurement conditions.

2.2 Natural resonant phenomena of ECT coil

Any of the coils always exhibit an inductive property because of the magnetic fields around them by applying a current into the coil. However, any of the coils have the capacitances among the coils. Even though a simple finite length solenoid coil shown in Fig. 1(a), it is possible to observe its natural resonance phenomena as shown in Fig. 2. Figs 2(a) and 2(b) are the frequency f versus impedance $|Z|$ and the frequency f versus phase ϕ characteristics, respectively.



(a) Impedance $|Z|$ vs. Frequency f .



(b) Phase ϕ vs. Frequency f .

Fig.2 Frequency characteristics of the impedance and phase.

2.3 Optimum operation frequency

Decision of ECT operation frequency is of paramount importance, because sensibility and searching depth of ECT are greatly depending on the operation frequency. Theoretically, the operation frequency of ECT can be decided by taking the target conductivity and its skin-depth into account. However, final selection of operation frequency is determined by the past experiences and the practical tests.

In the present paper, we select the natural parallel resonant frequency of the ECT sensor coil when facing with a wholesome part of target. The ECT facing with the wholesome part of target takes the maximum pure resistive impedance. When the ECT sensor coil meets with a defect of target, the resonance condition is essentially not established. Therefore, the input impedance from sensor coil input terminals is also reduced to small in value compared with those of the resonant one. Namely, a deviation between the resonance and not resonance impedances becomes maximum value.

A sensibility ϵ of ECT is defined by

$$\varepsilon = \frac{|reference - measured|}{reference} \times 100[\%], \quad (1)$$

where the reference and measured in (1) refer to the input impedances from the ECT coil terminals when facing the ECT coil with the wholesome and defect parts of target, respectively.

2.4 Enhancement of quality factor Q

The sensibility of (1) is greatly depended on the quality factor Q of the parallel resonance defined by

$$Q = \frac{f_0}{\Delta f}, \quad (2)$$

where f_0 and Δf are the resonant frequency and the bandwidth, respectively.

The quality factor Q represents a sharpness of the resonant curve on the impedance versus frequency coordinate. So that high Q in (2) means high sensibility in (1).

To increase the quality factor Q, we employ the resonant connection shown in Fig. 3. Figs. 3(a) and 3(b) are the two

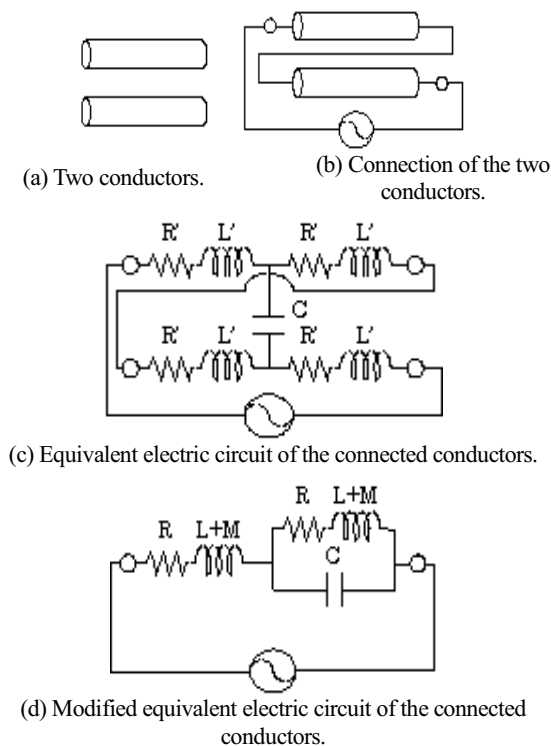


Fig.3 Principle of a resonance coil connection.

parallel conductors and their resonant connection, respectively. Denoting R, L, M as the resistance, self-inductance and, mutual inductance, it is possible to draw an equivalent circuit of the resonant connected two conductors as shown in Figs. 3(c), 3(d). Fig.4 shows a difference between the normal and resonant coil connection [4]. Practically, the resonant connection is carried out by twisting the two coils to uniform the facing side of both conductors as shown in Fig. 5 [5].

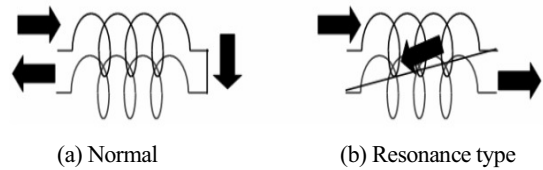


Fig.4 Comparison of the normal with resonant coil connections.



Fig. 5 Example of a pair of twisted coils

3 Experiment

3.1 Tested target peace and trial ECT coils

Fig. 6 shows a target peace which is composed of the two different types of materials (SUS304 and SUS316). A vertical line shape artificial crack having 10mm length, 0.2mm width and 0.5mm depth had been made to the sandwiched SUS by the electrical discharge machining. Fig. 6 shows a 20mm by 20mm target area. The ECT sensors measured at the 9 by 9 sampling points with 2.5mm regular spacing on this 20mm by 20mm square area.

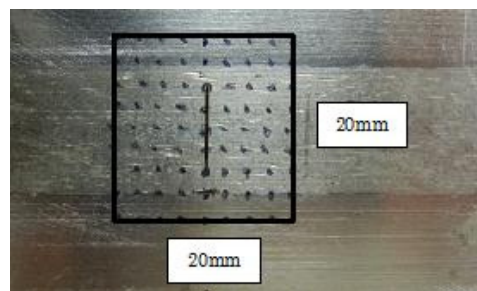


Fig. 6 Target test piece and measured points.

The test peace is composed of the two different types of SUS materials. A line shape artificial crack having 10mm length, 0.2mm width and 0.5mm depth had been made to the sandwiched SUS by the electrical discharge machining. A 20mm by 20mm square area is measured at the 9 by 9 points with 2.5mm regular spacing sampling

We have worked out a lots of ECT coils for comparison. Table 1 lists the representative 6 tested ECT coils. Every tested coil is wound around the Manganese-Zinc type ferrite bar used as an axial core material. No.1 is a normal ECT, No. 2 is a resonance type not employing twisting of coil, No.3 is a resonance type employing 100/m twisting, No.4 is a resonance type employing 150/m twisting, No.5 is a resonance type employing 200/m twisting, and No.6 is a resonance type employing 400/m twisting.

Table 1. Specification of the trial ECT coils.

No.	Type	Conductor length	Diameter of conductor	Axis core	Ferrite bar (MnZn)	Coil outer diameter	Coil inner diameter	Coil length	Number of twisted turns	Number of coil layers
No.1	Normal	50cm	0.1mm	Ferrite bar (MnZn)		2.4mm	2mm	6mm	0	2
No.2	Resonant	50cm	0.1mm	Ferrite bar (MnZn)		2.4mm	2mm	6mm	0	2
No.3	Twisting	50cm	0.1mm	Ferrite bar (MnZn)		3mm	2mm	5mm	100/m	3
No.4	Twisting	50cm	0.1mm	Ferrite bar (MnZn)		3mm	2mm	5mm	150/m	3
No.5	Twisting	50cm	0.1mm	Ferrite bar (MnZn)		3mm	2mm	5mm	200/m	3
No.6	Twisting	50cm	0.1mm	Ferrite bar (MnZn)		3mm	2mm	5mm	400/m	3

3.2 Conventional ECT operating at 256kHz

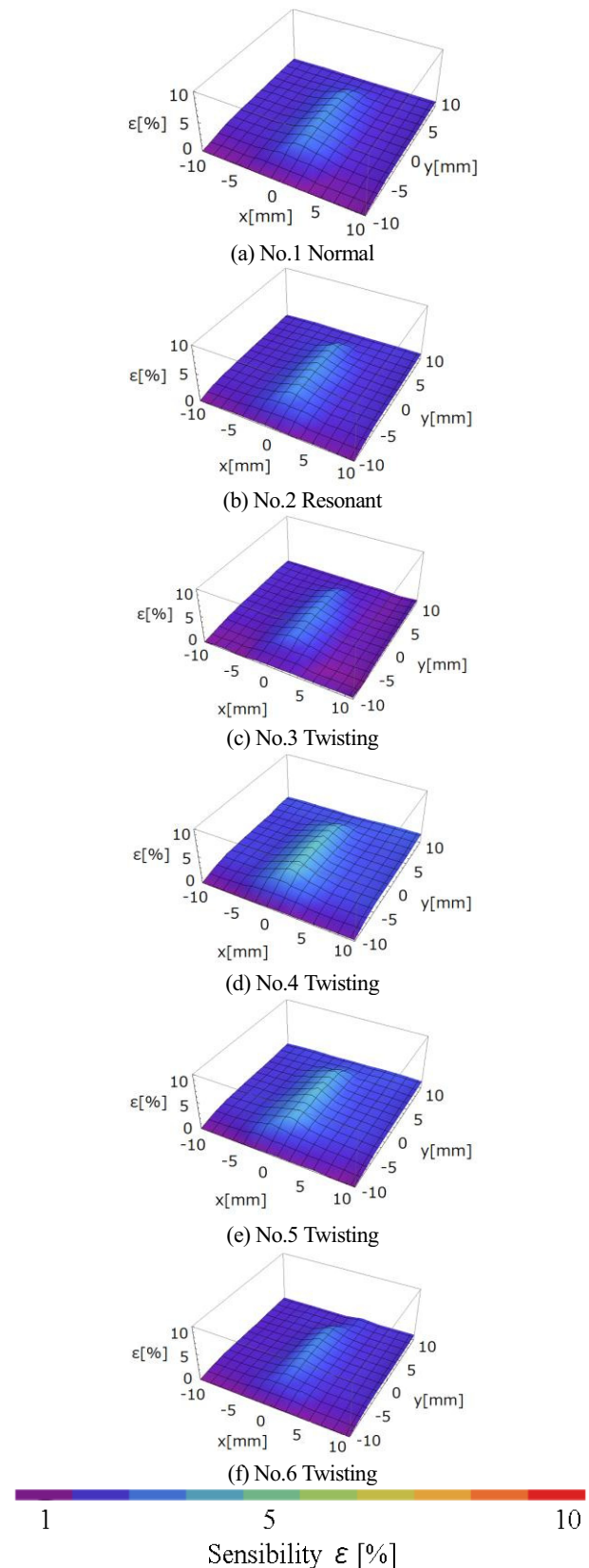


Fig. 7 Defect searching results. Any sensor coils can detect the two different kinds of base metallic materials.

At first, we evaluated the line shape crack in Fig. 6 by conventional ECT employing 256kHz operating frequency. Fig.7 shows the results of defect searching. Observe the results in Fig. 7 suggests that any of the sensor coils are capable of detecting the two different kinds of base metallic materials. Further, it is difficult to decide which sensor is the highest sensibility. In the other words, normal ECT defect searching using a particular operating frequency never reflects on the difference of the conductor connection and coil twisting.

3.3 ECT operating at resonant frequency

Any types of ECT coils have their own natural resonant frequency even if they are facing with the target without any defect. No.1,2,3,4,5 and 6 ECT coils in Table 1 have the natural resonant frequencies, 4650, 4950, 3650, 3300, 3425 and 3475 kHz, respectively. Fig. 8 shows the typical frequency characteristics of the trial ECT coils.

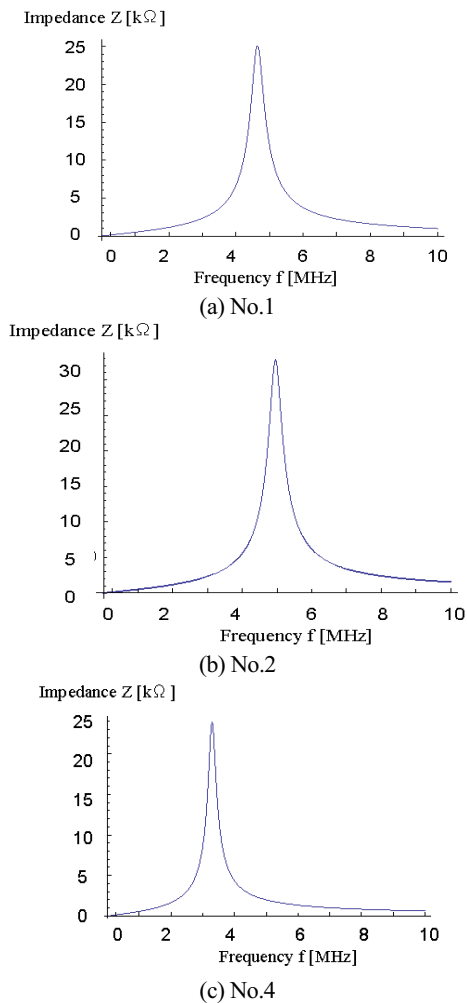


Fig. 8 Frequency f vs. impedance $|Z|$ characteristics of the ECT coils (a) No.1, (b) No.2 and (c) No.4, respectively.

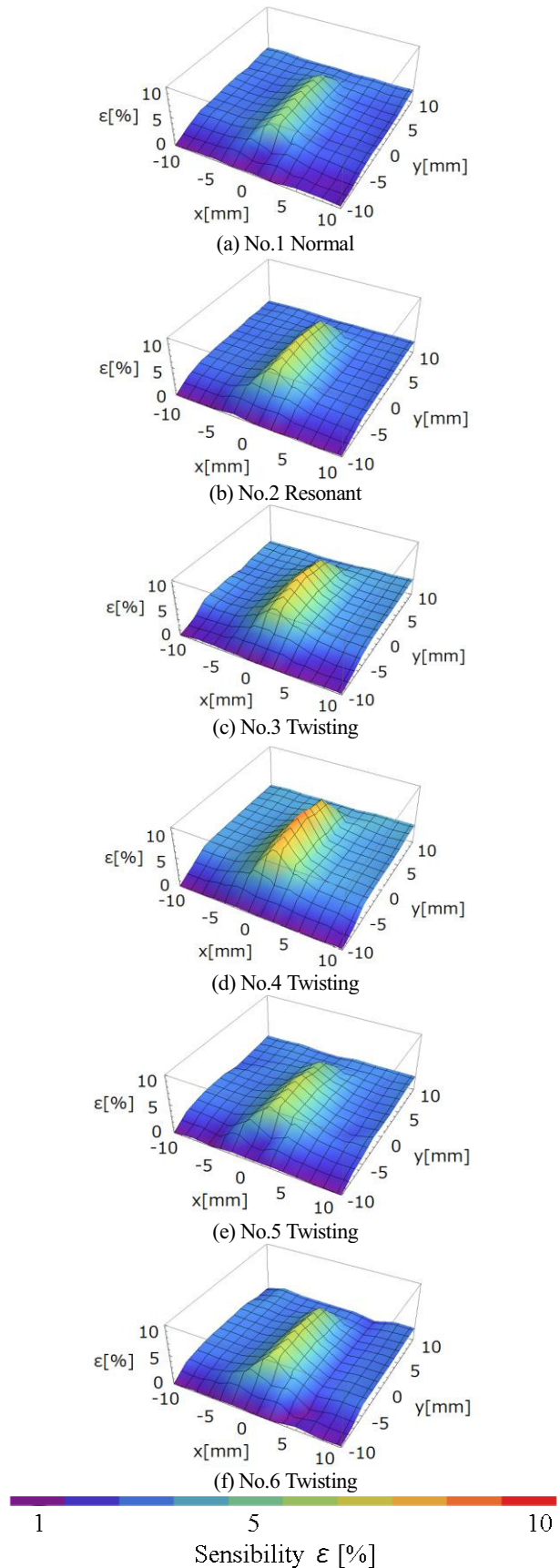


Fig. 9 The results of defect searching. Any sensor coils can detect two different kinds of base metallic materials.

Fig. 9 shows the defect searching result using each of the distinct natural resonant frequencies. Comparison of the results in Fig. 7 with that of Fig. 9 reveals that the resonant frequency operation is far superior sensibility in any ECT coils. In particular, No. 4 in Fig. 9(d) exhibits nearly 10% deviation. This fact is verified that the quality factor of No.4 in Fig. 9(b) is far excellent compared with those of No.1 and of No.2.

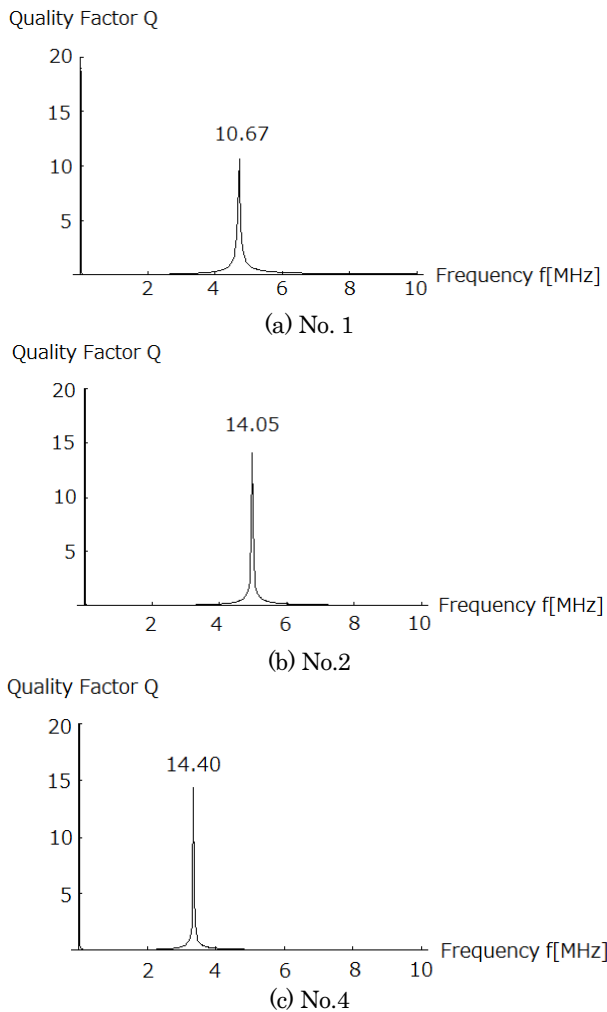


Fig. 10 Comparisons among the Quality Factor Q of the No.1, No.2 and No.4 ECT coils.

4 Conclusion

New innovative idea to enhance the sensibility of ECT sensor has been proposed in this work. Our idea needs not any special tools but requires a consideration of natural resonance phenomena-, i.e., utilization of the resonant impedance, frequency and capacitive effect among the coils.

We have selected the natural parallel resonant frequency of the ECT sensor coil when facing with a wholesome part of target. When the ECT sensor coil has met with a defect of

target, the resonance condition has not been established. This has led that the impedance has reduced to small value compared with those at resonant condition. As a result, a deviation between the resonant and not resonant impedances has become the maximum. Thus, the sensibility of ECT sensor has been enhanced.

Further, connection of the conductors to be applied a half of the source voltage to adjacent conductors has made it possible to enhance the capacitive effect among the conductors. Practically, this connection has been carried out by twisting the two coils to uniform the facing side of both conductors. Due to this enhancement of the capacitive effects, the resonant frequency has been reduced and succeeded in increasing the sensibility.

References

- [1] I.Marino, S.Hayano and Y.Saito, Ployphase eddy current testing, *Journal of Applied Physics*, Vol. 75, No.10, pp. 5904-5906, 1994.
- [2] N.Burais and A.Nicolas, Electromagnetic field analysis in remote field eddy current testing systems, *IEEE Transactions on Magnetics*, Vol.25, No.4, pp.3010-3012, 1989.
- [3] S.McFee and J.P.Webb, Automatic mesh generation for h-p adaption, *IEEE Transactions on Magnetics*, Vol.29, No.2, pp.1894-1897, 1993.
- [4] Y.Midorikawa, S.Hayano and Y.Saito, A resonant phenomenon between adjacent series connected coils and its application to a als, *Advanced Computational and Design Techniques in Applied Electromagnetic Systems*, Vol.6, pp. 633-639, 1995.
- [5] S.Hayano, Y.Nakajima, H.Saotome and Y.Saito, A new type high frequency transformer, *IEEE Transactions on Magnetics*, Vol. 27, No.6, pp.5205-5207, 1991.

Fluctuation Frequency Analysis of the Barkhausen Signals

Jun KAWAZOE^{*1}, Iliana Marinova^{*2} and Yoshifuru SAITO^{*1}

^{*1} Graduate School of Hosei University, Tokyo 184-8584, Japan

^{*2} Technical University of Sofia, Sofia 1756, Bulgaria

Ferromagnetic materials are widely used for various artificial products such as cars, trains, ships and so on. Because of its mechanical property, iron steel is most popular in use for the frame materials. Nondestructive testing of iron steel is an extremely important way to maintain their mechanical reliability. As is well known fact that the Barkhausen signals are emitted from only the ferromagnetic materials having magnetic domain structures. Also this signal varies depending upon their past mechanical as well as radioactive stress histories.

In the present paper, we have applied a generalized frequency fluctuation analysis to the Barkhausen signals to detect the various mechanical stresses. Surprisingly, it has been succeeded in clarifying that application of our frequency fluctuation analysis to the Barkhausen signals makes it possible to detect the several kinds of mechanical stress.

Key words: Barkhausen signal, Frequency fluctuation, Signal processing, Least squares

1. Introduction

Barkhausen signal is popularly observed in the ferromagnetic materials composed of the magnetic domain structures, e.g. iron, nickel, cobalt and garnet, when they are magnetizing. Also, it is well known that the Barkhausen signals are very sensitive to the physical external input, such as mechanical stress and radioactive damage, to the ferromagnetic materials.

The iron and its composite ferromagnetic materials are widely used for main frame materials to support the mechanical structures in many artificial products and constructions. Because of their essential role, they are always got mechanical stress and they keep their past mechanical stress histories. Nondestructive detection of their mechanical stress as well as residual stress is of paramount importance for keeping the safety of the mechanical structures, since it is possible to see ahead of time what extent the mechanical structure will maintain their strength for further use.

According to the past researches concerning to a relationship between the Barkhausen signal and applied mechanical stress, it has been revealed that Barkhausen signals are very sensitive to the mechanical stress and radioactive damage but any deterministic regularity has not been found [1,2].

Recently, only a macroscopic regularity has been reported by means of a frequency fluctuation analysis approach [3]. Principal purpose of this paper is that conventional frequency fluctuation analysis employing only 1st order fluctuation is generalized to the frequency fluctuation analysis employing the n^{th} order fluctuations.

As a result, we succeed in extracting the distinct difference between the stressed and not stressed Barkhausen signals. Also, we succeed in visualizing in a most clear manner on the four dimensional space, whose coordinates are composed of the terms representing the higher order frequency fluctuation terms of Barkhausen signals.

One of the most famous frequency fluctuations is the 1/f frequency fluctuation, which can be observed in most of the natural phenomena such as natural wind, sea water waves, river flow sound and so on gives a healing effect to the mentalities via human sensibilities[4].

Conventional 1/f frequency analysis is that application of the 1st order least squares to the both Fourier power spectrum and frequency extracts the 1st order frequency fluctuation, i.e., Log of Fourier power spectrum is approximated by Log of $a_0 + a_1/f$, yields a 1st order frequency fluctuation characteristic, where a_0 and a_1 are the 0th and a 1st order frequency fluctuation terms, respectively. If the frequency fluctuation term a_1 takes $a_1=1$, then we have the 1/f frequency fluctuation.

On the other side, we generalize this conventional 1st order frequency fluctuation to the n^{th} order frequency fluctuation characteristics, i.e., Log of Fourier power spectrum is approximated by a Log of $a_0 + a_1/f + a_2/f^2 + \dots + a_n/f^n$, where $a_0, a_1, a_2, \dots, a_n$ are the 0th, 1st, 2nd, ... , n^{th} order frequency fluctuation terms, respectively. Careful examination of the coefficients $a_0, a_1, a_2, \dots, a_n$ leads to the precise frequency fluctuation characteristic of the Barkhausen signal.

Second important key point of our approach is how to visualize the dependency of the 0th, 1st, 2nd, ... , n^{th} order frequency fluctuation terms to the externally applied forces.

According to our experimental results on this research, most of the frequency fluctuation characteristics are sufficiently represented up to the 4th order terms. So that let the normalized 1st, 2nd, 3rd, 4th order frequency fluctuation coefficients be respectively the coordinate values on the x-, y-, z-axes, and point color, then up to the 4th order frequency fluctuation characteristics locate the three dimensional space coordinate position and point color. Thus, comparison among the different specimens of this diagram visualizes an each of the distinct characteristics depending on their mechanical stress conditions.

2. Frequency Fluctuation Analysis

2.1 Basic equations

Let us consider an arbitrary signal $g(t)$ and its Fourier power spectrum $G(f)$, and take the logarithm of both Fourier Spectrum $G(f)$ and frequency f . Plot the $\log G(f)$ on the $\log f$ coordinate represents a frequency characteristic of the signal $g(t)$ on the frequency domain, i.e., the frequency characteristic of the original signal is represented on a x - y plane coordinate system whose horizontal x - and vertical y -axes are corresponding to the logarithms of Fourier power spectrum $G(f)$ and of frequency f , respectively.

In order to represent a global frequency characteristic of the original signal $g(t)$ in frequency domain, apply a following power series function:

$$h(f) = a_0 + a_1 f + a_2 f^2 + \dots + a_n f^n, \quad (1)$$

in this x - y plane makes it possible to evaluate the higher order frequency fluctuation analysis.

The coefficients $a_0, a_1, a_2, \dots, a_n$ in (1) are determined by least squares as

$$\mathbf{A} = [\mathbf{C}^T \mathbf{C}]^{-1} \mathbf{C}^T \mathbf{Y}, \quad (2)$$

where a superscript T denotes a matrix transpose; the vectors \mathbf{A} , \mathbf{Y} and matrix \mathbf{C} are respectively given by

$$\mathbf{A} = [a_0 \quad a_1 \quad \dots \quad a_n]^T, \quad (3)$$

$$\mathbf{Y} = [h(f_0) \quad h(f_1) \quad \dots \quad h(f_m)]^T, \quad (4)$$

$$\mathbf{C} = \begin{bmatrix} 1 & f_0 & f_0^2 & \dots & f_0^n \\ 1 & f_1 & f_1^2 & \dots & f_1^n \\ 1 & f_2 & f_2^2 & \dots & f_2^n \\ \dots & \dots & \dots & \dots & \dots \\ 1 & f_m & f_m^2 & \dots & f_m^n \end{bmatrix}, \quad (5)$$

$$m > n.$$

In (3)-(5), a number of equations m , i.e. number of the sampled frequencies $f_0, f_1, f_2, \dots, f_m$, always greater than those of unknowns n , i.e., number of the coefficients $a_0, a_1, a_2, \dots, a_n$. In most case, this condition is satisfied because of the number of sampled frequency m is much greater than those of the order n of the function $h(f)$ in (1).

2.2 Classical 1st order frequency fluctuation

Fig. 1 shows a Barkhausen signal measurement devices.

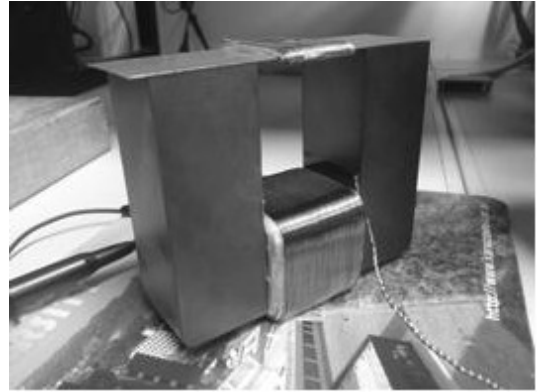


Fig.1. Barkhausen signal measurement devices.

The tested specimens are the silicon steels with the 0.35mm thickness, 30mm width and 100mm length. The tested specimen is put on the upper two head surfaces of U shape ferrite core wound the 300 turns exciting coil. The specimen in Fig.1 is excited by flowing a 1A sinusoidal alternating current through this exciting coil.

Fig. 2 shows a typical frequency characteristic of a Barkhausen signal under no stress.

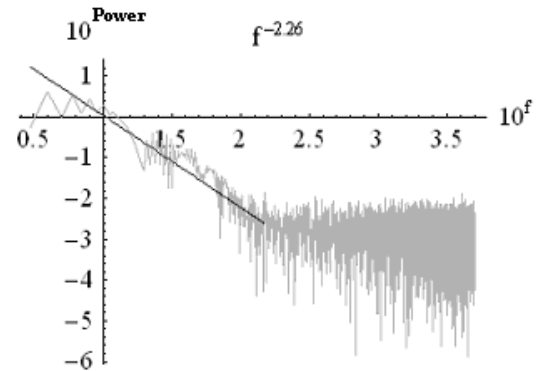


Fig. 2. An example of typical frequency characteristic of a Barkhausen signal under no stress.

The frequency characteristic in Fig. 2 is obviously divided into two frequency regions. One is lower frequency region whose frequency fluctuation can be approximated by $f^{2.26}$ derived from 1st order approximation in (1), and the other higher one is a dispersing signal whose frequency fluctuation can be approximated by f^0 , i.e. white noise.

On the other side, Fig. 3 show a typical frequency characteristic of Barkhausen signal under 3kg stressed.

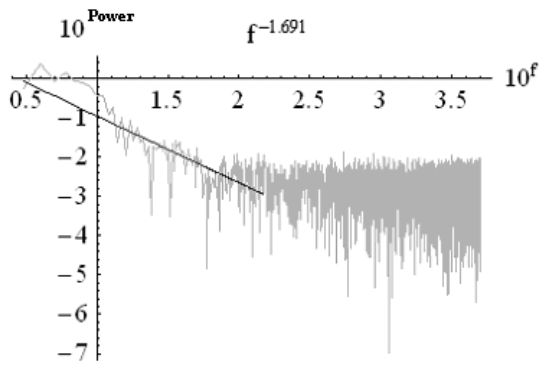


Fig. 3. An example of typical frequency characteristic of a Barkhausen signal under 3kg stressed.

The frequency characteristic in Fig. 3 is also divided into the two frequency regions. One is lower frequency region whose 1^{st} order frequency fluctuation can be approximated by $f^{1.69}$, and the other higher one is a dispersing signal whose frequency fluctuation can be approximated by f^0 .

Consideration to the difference between the first order fluctuations $f^{2.26}$ and $f^{1.69}$ suggests that an application of the 3kg stress to the tested silicon steel changes the steep 1^{st} order gradient -2.26 to the smoothly gradient -1.68. This result had been verified by the 1^{st} order frequency fluctuation analysis to the 30 distinct sample specimens [3].

Thus, it is possible to detect the stress on the ferromagnetic materials by the classical 1^{st} order frequency fluctuation analysis [3].

However, several difficulties are still remaining: One is how to decide the frequency range to be computed the frequency fluctuation characteristic. Second is that the 1^{st} order frequency fluctuation analysis is only effective to a relatively large stress, even though it is required to detect the much more smaller stresses.

2.3 Generalized frequency fluctuation

Fig. 4 shows a frequency fluctuation characteristic under no stress along with a curve obtained by up to the 4^{th} order power series function in (1), where the frequency sampling points have been taken in a logarithmic order.

To check the reproducibility of the coefficients a_1, a_2, a_3, a_4 , we have 10~12 times independently measured and computed these coefficients a_1, a_2, a_3, a_4 in (1) to the same specimen.

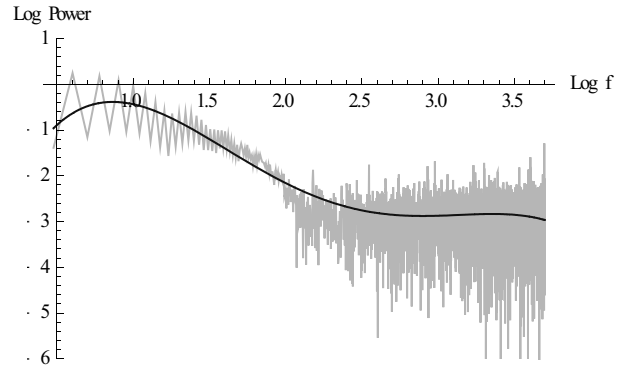
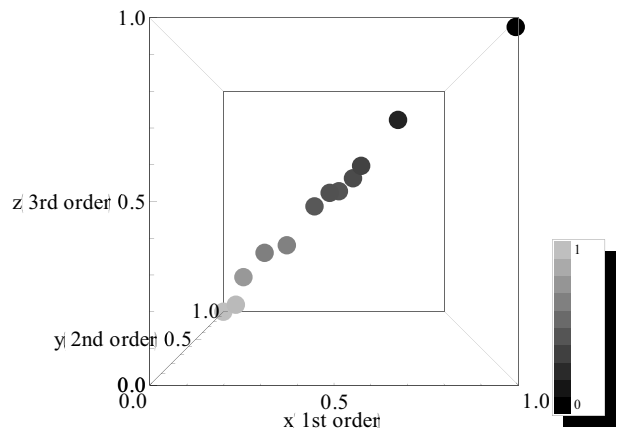
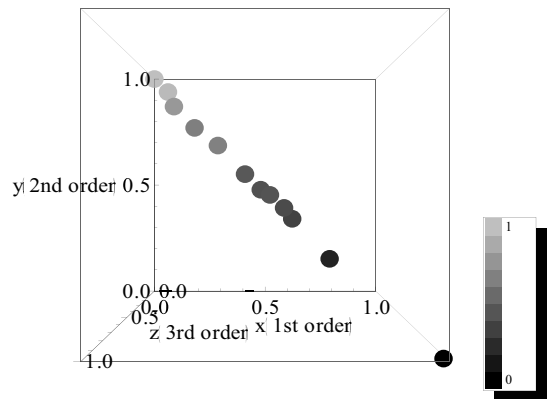


Fig. 4. Example of typical frequency characteristic of a Barkhausen signal under no stress along with an up to 4^{th} order power series curve in (1).

After normalizing all of the coefficients a_1, a_2, a_3, a_4 to be the values between 1 and 0, let the normalized coefficients a_1', a_2', a_3', a_4' be respectively corresponded to the x-, y-, z-axes values and point color, then this makes it possible to visualize a dispersion characteristic of the coefficients a_1', a_2', a_3', a_4' . Fig. 5 shows a dispersion characteristic of these coefficients a_1', a_2', a_3', a_4' . Combination of Figs. 5(a) with 5(b) reveals that the dispersion is limited along the vicinity of a hatched surface in Fig. 6.



(a) x-y plane



(b) x-z plane

Fig.5. Dispersion of the frequency fluctuation coefficients.

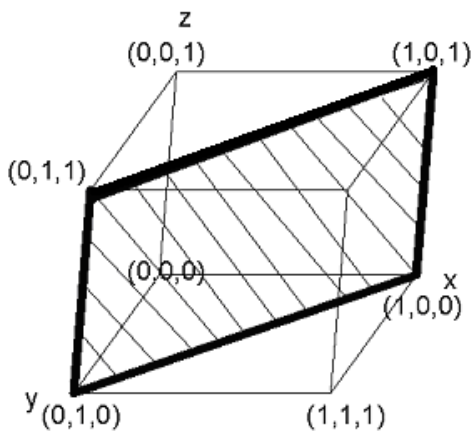


Fig.6. The normalized frequency fluctuation coefficients a_1', a_2', a_3', a_4' dispersing area (hatched surface).

Consideration to the hatched region in Fig. 6 suggests that an individual difference among the sound silicon steel without any stresses could be limited along the vicinity of the hatched surface in Fig. 6.

2.4 Stress visualization

We have carried out the random stresses visualization in much the same as described in Section 2.3. These stresses were applied to the specimen by hanging the random weights by a string as shown Fig. 7.

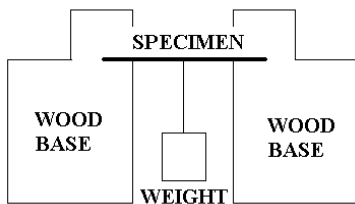


Fig.7. The stresses are applied by hanging the weights.

Fig. 8 shows one of the frequency fluctuation characteristics under stress along with a curve obtained by the 4th order power series function in (1).

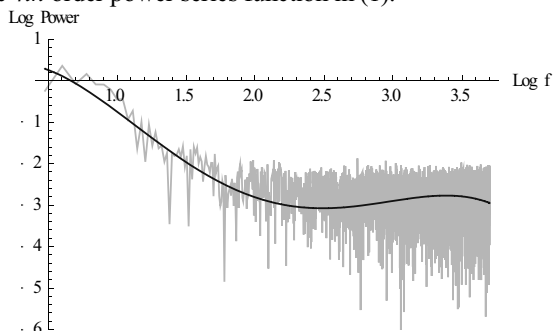


Fig. 8. One of the frequency characteristic of the Barkhausen signals under stress along with the 4th order power series curve in (1).

Fig. 9 shows the dispersion characteristics of coefficients a_1', a_2', a_3', a_4' .

Comparison of the dispersion characteristics in Fig. 5(a) with that of Fig. 9(a) demonstrates a distinct effect of the applied stress. Also, comparison of the dispersion characteristics a_1', a_2', a_3', a_4' in Fig. 5(b) with that of Fig. 9(b) suggests the same as before.

Combination of Figs. 9(a) and 9(b) yields the results shown in Figs. 10 and 11.

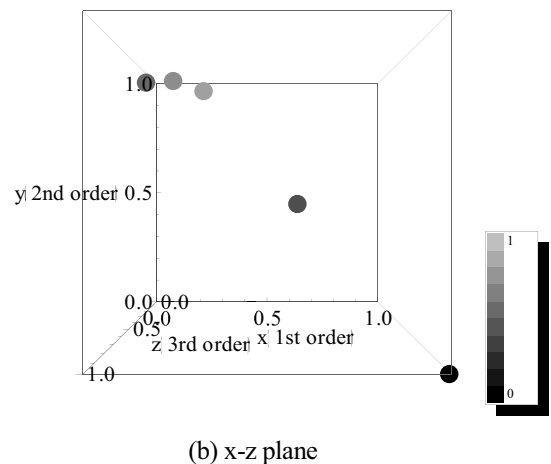
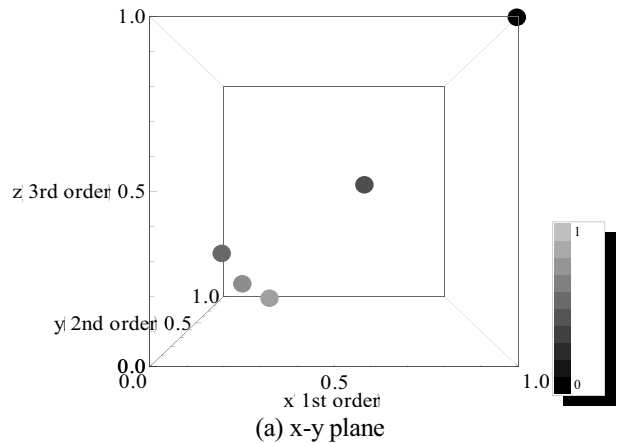


Fig.9. Dispersion of the frequency fluctuation coefficients.

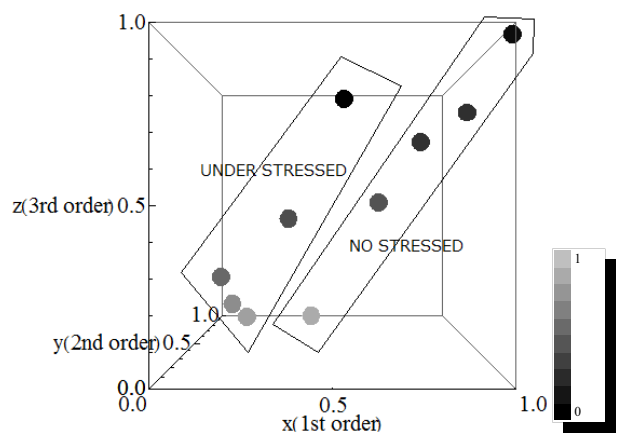


Fig. 10. The normalized frequency fluctuation coefficients a_1', a_2', a_3', a_4' difference between the stressed and no stressed groups on the x-y plane.

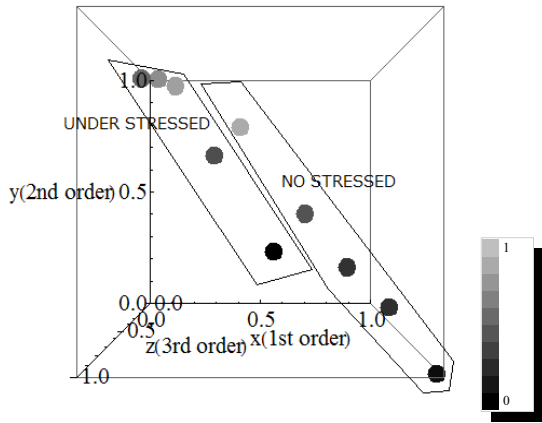


Fig. 11. The normalized frequency fluctuation coefficients a_1', a_2', a_3', a_4' difference between the stressed and no stressed groups on the x-z plane.

Observation of the dispersion characteristics of the stressed specimens suggests that the normalized coefficients a_1', a_2', a_3', a_4' in (1) do not disperse but focus on a relatively small area. On the contrary, the normalized coefficients a_1', a_2', a_3', a_4' in (1) of the stress free specimens disperse the vicinity of hatched area in Fig. 6. This means that the externally applied stress suppresses the dispersion and confines them into the small space in Fig. 6.

2.5 Bending effect visualization

We have carried out the bending effect visualization in much the same as described in Section 2.4.

As shown the bended examples in Fig. 12, the 4 specimens were bended 0, 5, 15, and 45 degree. After that these 4 specimens were recovered to the original straight form.

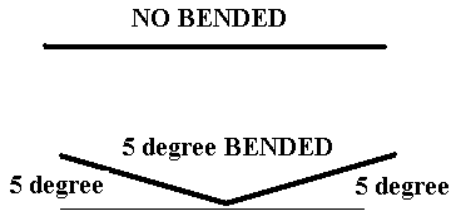


Fig. 12. No bended and 5 degree bended.

Fig. 13 shows one of the frequency fluctuation characteristics after bending along with a curve obtained by the 4th order power series function in (1).

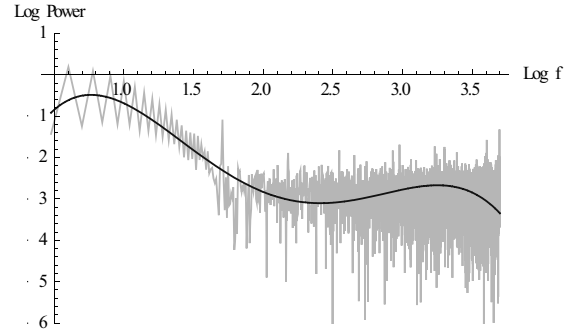
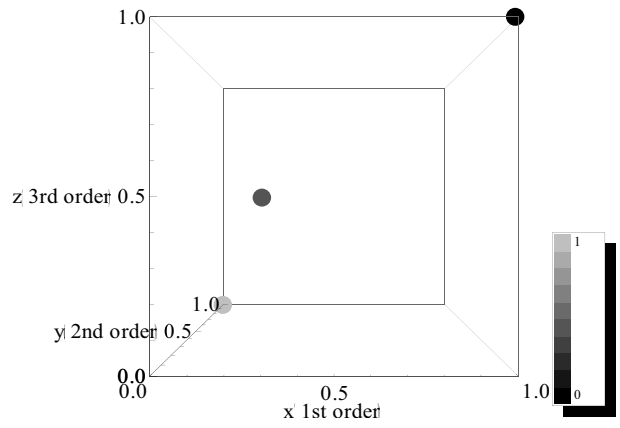
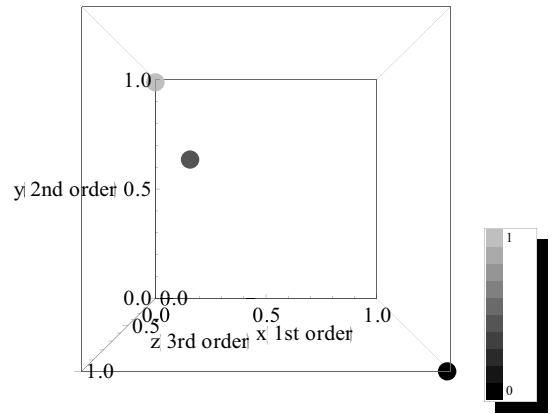


Fig. 13. One of the frequency characteristics of the Barkhausen signal after bending a specimen along with the 4th order power series curve in (1).



(a) x-y plane



(b) x-z plane

Fig.14. Dispersion of the frequency fluctuation coefficients.

Fig. 14 shows the normalized dispersion characteristics of coefficients a_1', a_2', a_3', a_4' .

Comparison of the dispersion characteristics in Fig. 5(a) with that of Fig. 14(a) demonstrates a distinct effect of the bending. Also, comparison of the dispersion characteristics in Fig. 5(b) with that of Fig. 14(b) suggests the same as before.

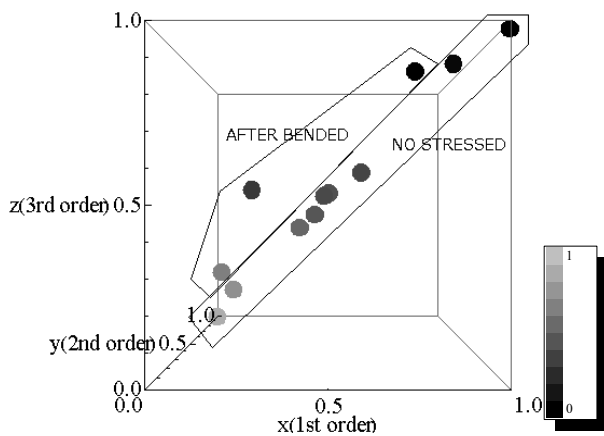


Fig. 15. The normalized frequency fluctuation coefficients a_1', a_2', a_3', a_4' difference between the bending and not bending groups on the x-y plane.

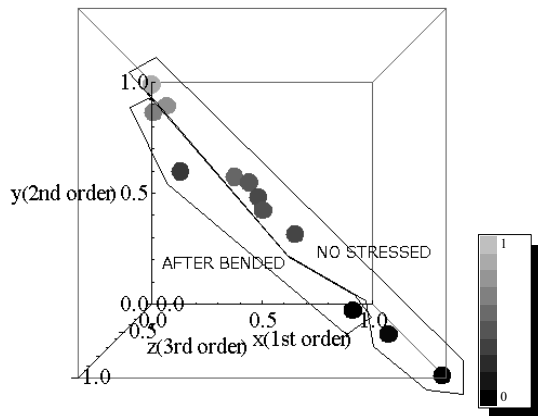


Fig. 16. The normalized frequency fluctuation coefficients a_1', a_2', a_3', a_4' difference between the bending and not bending groups on the x-z plane.

Combination of Figs. 14(a) and 14(b) yields the results shown in Figs. 15 and 16.

Observation of the dispersion characteristics of the bended specimens suggests that the normalized coefficients a_1', a_2', a_3', a_4' in (1) do not disperse but focus on a relatively small area. On the other side, the normalized coefficients a_1', a_2', a_3', a_4' in (1) of the bended free specimens disperse the vicinity of the hatched surface in Fig. 6. Thereby, the externally applied bending stress suppresses this dispersion and confines them into the small space in Fig. 6.

Thus, it is obvious that the distinction between the stressed and bending effects is difficult from the Barkhausen signal analysis.

3. conclusion

Previously, we have succeeded in detect the applied stress on the silicon steel by means of the frequency fluctuation method [3].

This paper has generalized this approach, i.e., 1^{st} order to the n^{th} order frequency fluctuations. Further, the 4^{th} order

frequency fluctuation characteristics could be visualized in a three dimensional space. This has clarified each of the distinct differences among the specimen having the same specifications, also clarified the measurement data dispersions.

As the concrete examples, we have applied our method to the stress visualization of the silicon steels, and succeeded in extracting the characteristics of the stressed specimens. Also, we have applied our method to the past bended history detection. This has led to the similar results obtained in the stress detection. Thereby, it has been clarified that the distinct difference between the past stressed or bended histories is difficult.

References

- [1] R M. Bozorth: Ferromagnetism, p. 462 (IEEE PRESS)
- [2] M. Katsumata, S. Hayano and Y. Saito: A Study of Barkhausen Phenomenon Visualization, *The Visualization Society of Japan*, B203, July (2003).
- [3] S. Nojima and Y. Saito: Application of Frequency Fluctuation to Barkhausen Signals and its Application, *J. Magn. Soc. Jpn.*, 35, 380-385 (2011).
- [4] M. Teranishi, K. Maruyama, S. Hayano, and Y. Saito: Visualization of $1/f$ Frequency Component in Dynamic Image of Natural Phenomena, *The Visualization Society of Japan*, B108, July (2005).

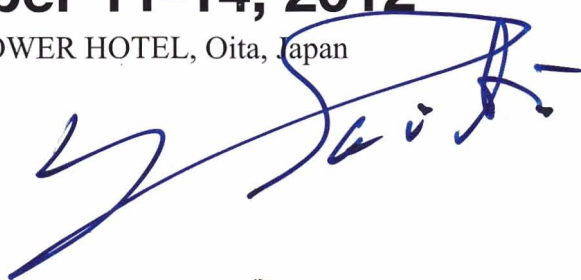
Digests of the 15th Biennial IEEE Conference on Electromagnetic Field Computation (CEFC2012),
November 11-14, 2012, Oita Oasis Tower Hotel, Oita, Japan

CEFC2012

The 15th Biennial IEEE Conference
on Electromagnetic Field Computation

November 11-14, 2012

OITA OASISTOWER HOTEL, Oita, Japan



Coupled Field Modeling of Ferrofluid Heating in Tumor Tissue

Valentin Mateev¹, Iliana Marinova¹ and Yoshifuru Saito²

¹ Technical University of Sofia, Sofia 1756, Bulgaria

² Graduate School of Hosei University, Tokyo 184-8584, Japan

vmateev@tu-sofia.bg

Abstract — In this work, method of magnetic fluid hyperthermia is implemented for breast cancer therapy. Coupled field modeling of ferrofluid transport and heating in tumor tissue is presented. A forward 3D electromagnetic – thermal - fluid dynamics, finite element method model is developed. The model uses anatomically precise multilevel geometrical model of human breast with known tissues electrical properties, blood and liquor flow speeds in its vessels. The model presents the structure of real cancer sample acquired by surgical procedure. Cancer and normal tissue electrical properties are directly measured for this sample. Thermal field results are verified by infrared thermograph imaging.

I. INTRODUCTION

The method of magnetic fluid hyperthermia selectively heats up tissues by inducted alternating current to targeted magnetic fluid [1-2]. Magnetic fluid distribution determines thermal field inside tissues under therapy process. Inversely magnetic fluid transport and distribution rearranges electromagnetic field which can dramatically change thermal field in that sensitive live tissue domain. Otherwise anatomy objects under investigation are particularly complex structures, which are often non rigid and random in shape, and exhibit considerable variability from person to person. Tissues electromagnetic and thermal properties are anisotropic, frequency and time varying and in general are not clearly determined for all tissues in case under investigation. All of this as well as an absence of explicit shape models that capture anatomy specifics, makes modeling task challenging.

In this work, coupled field modeling of ferrofluid transport and heating in tumor tissue is presented. A forward 3D electromagnetic – thermal - fluid dynamics finite element method (FEM) model is developed.

II. METHOD

For determination of the thermal field distribution in magnetic hyperthermia therapy, a coupled electromagnetic – thermal - fluid dynamics field model is established. The electromagnetic field distribution inside the conductive tissue region depends on the time varying magnetic flux density. The heat sources are defined by the electric losses in tissue, acquired by the solution of the electromagnetic field problem. The analysis was carried out on a three-dimensional transient electromagnetic problem according FEM formulation.

The FEM model uses anatomically precise multilevel geometrical model of human breast with known tissues electrical properties, blood and liquor flow speeds in its vessels. Model contains information about real cancer structure sample acquired by surgical procedure. Cancer and normal tissue electrical properties are directly measured for

this sample by precise measurement system [3]. According to frequency dependent properties of the dataset, shown in Fig.1, thermal conductivities, for all tissues types included in the model are defined.

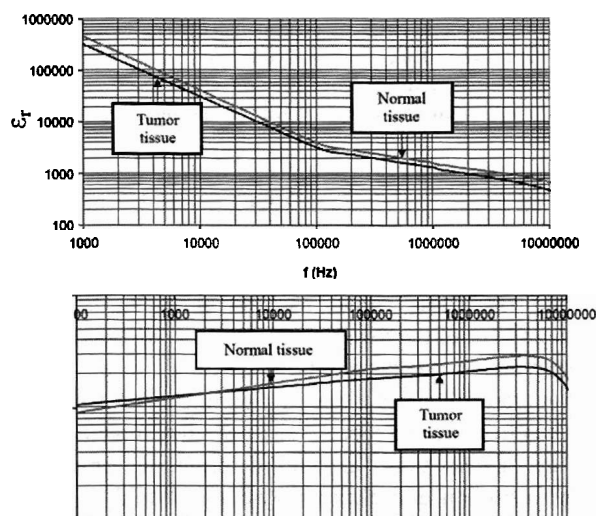


Fig. 1. Measured relative electric permittivity - ϵ' and electric conductivity - σ of cancer tissue samples.

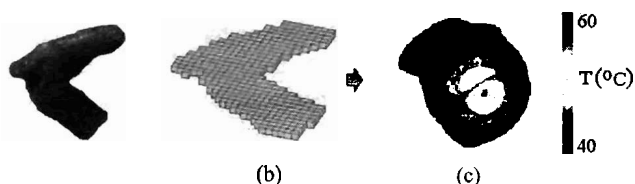


Fig. 2. Sample shape (a), layer of cancer model (b) and surface thermal field distribution in breast model (c).

Fig. 2 shows the structure of real cancer sample acquired by surgical procedure. The 3D geometry model of same cancer structure reconstructed for the model is shown in Fig. 2(b). Calculated thermal field distribution in the breast is demonstrated in Fig.2(c).

III. REFERENCES

- [1] A. Golneshana and M. Lahonian, "Diffusion of magnetic nanoparticles in a multi-site injection process within a biological tissue during magnetic fluid hyperthermia using lattice Boltzmann method", *Mechanics Research Communications*, Vol. 38, pp. 425–430, 2011.
- [2] M. Liangruksa, R. Ganguly and I. Puri, "Parametric investigation of heating due to magnetic fluid hyperthermia in a tumor with blood perfusion," *Journal of Magnetism and Magnetic Materials*, Vol. 323, pp. 708–716, 2011.
- [3] I. Marinova and V. Mateev, "Determination of Electromagnetic Properties of Human Tissues", *Proceedings of International Conference on Computational and Applied Mathematics*, 28-30 June, Paris, France, 2010, Vol. 66, pp. 1075-1079, 2010.

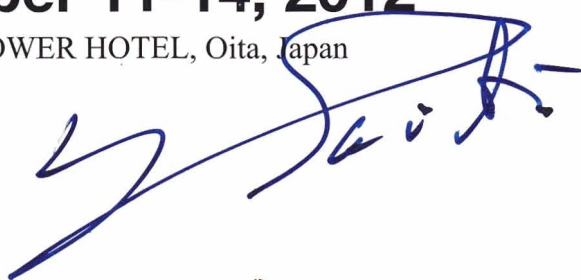
Digests of the 15th Biennial IEEE Conference on Electromagnetic Field Computation (CEFC2012),
November 11-14, 2012, Oita Oasis Tower Hotel, Oita, Japan

CEFC2012

The 15th Biennial IEEE Conference
on Electromagnetic Field Computation

November 11-14, 2012

OITA OASISTOWER HOTEL, Oita, Japan



Fluctuation Frequency Analysis of the Barkhausen Signals under Static and Dynamic Stresses

Jun KAWAZOE*, Iliana MARINOVA** and Yoshifuru SAITO*

*Graduate School of Electrical Engineering, Hosei University, 3-7-2 Kajinocho, Koganei, Tokyo 184-8584, Japan

**Technical University of Sofia, Sofia 1756, Bulgaria

Jun.kawazoe.9s@stu.hosei.ac.jp

Abstract— Most of the electromagnetic computation technologies for electrical machines design may be established even though the solid state physical properties of the ferromagnetic materials used as main constructing materials of the electrical machines are never fully taken into account.

This paper tries to compensate the current computational electrical machines design problem on the ferromagnetic materials. Namely, this paper tries to work out the evaluating methodology for which the electric machines are optimally designed or not by means of the Barkhausen signal analysis. Barkhausen signals are intrinsically accompanying with the magnetization processes of the ferromagnetic materials.

I. THE BARKHAUSEN SIGNAL ANALYSIS

Barkhausen signal is popularly observed in the ferromagnetic materials composed of the magnetic domain structures, e.g. iron, nickel, cobalt and garnet, when they are magnetizing. Also, it is well known that the Barkhausen signals are very sensitive to the physical external input, such as mechanical stress and radioactive damage to the ferromagnetic materials.

All of such ferromagnetic materials construct the major frame parts of electrical machines, even though the solid state magnetization properties of ferromagnetic materials are never fully taken the computational design of them into account. Because of their essential role, ferromagnetic materials are always got mechanical stress and they keep their past mechanical stress histories. Nondestructive detection of their mechanical stress as well as residual stress is of paramount importance for checking the properness of the mechanical structures, since it is possible to see ahead of time what extent the mechanical structure will maintain their strength for further use.

According to the past researches concerning to a relationship between the Barkhausen signal and applied mechanical stress, it has been revealed that Barkhausen signals are very sensitive to the mechanical stress and radioactive damage but any deterministic regularity has not been found [1,2].

Recently, only a macroscopic regularity has been reported by means of a frequency fluctuation analysis approach [3]. Principal purpose of this paper is that conventional frequency fluctuation analysis employing only 1st order fluctuation is generalized to the frequency fluctuation analysis employing the n^{th} order fluctuations.

As a result, we succeed in extracting and visualizing the distinct difference between the stressed and not stressed Barkhausen signals for the first time in the world.

Thus, it is revealed that our generalized frequency fluctuation analysis makes it possible to visualize the static as well as dynamic stresses to the ferromagnetic materials used in the electrical machines.

II. VISUALIZATION OF THE BARKHAUSEN SIGNALS

Fig. 1 shows one of the examples of frequency fluctuation characteristic under no stress along with a curve obtained by up to the 4th order power series function. Fig.2 shows a visualized result of the under no- and static-stressed Barkhausen signal characteristics.

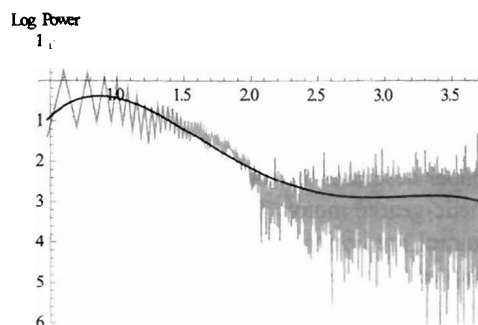


Fig. 1. Example of typical frequency characteristic of a Barkhausen signal under no stress along with an up to 4th order power series curve.

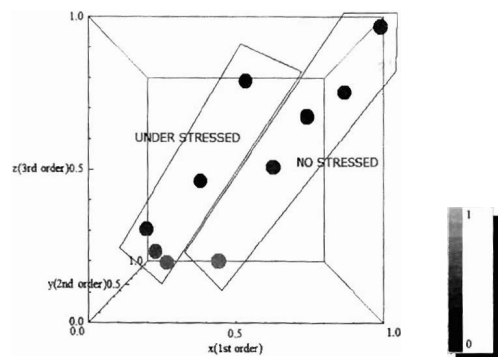


Fig. 2. The normalized frequency fluctuation coefficients difference between the stressed and no stressed groups.

III. REFERENCES

- [1] R M. Bozorth: *Ferromagnetism*, p. 462 (IEEE PRESS)
- [2] M. Katsumata, S. Hayano and Y. Saito: *A Study of Barkhausen Phenomenon Visualization*, The Visualization Society of Japan, B203, July (2003).
- [3] S. Nojima and Y. Saito: *Application of Frequency Fluctuation to Barkhausen Signals and its Application*, *J. Magn. Soc. Jpn.*, 35, 380-385 (2011).

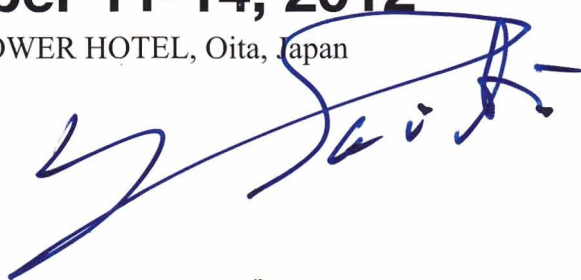
Digests of the 15th Biennial IEEE Conference on Electromagnetic Field Computation (CEFC2012),
November 11-14, 2012, Oita Oasis Tower Hotel, Oita, Japan

CEFC2012

The 15th Biennial IEEE Conference
on Electromagnetic Field Computation

November 11-14, 2012

OITA OASISTOWER HOTEL, Oita, Japan



IEEE



OITA
UNIVERSITY

<http://www.cefc2012.org/>

Optimization of the Eddy Current Testing

Hiroki KIKUCHIHARA¹, Iliana MARINOVA², Yoshifuru SAITO¹,
Manabu OHUCHI³, Hideo MOGI³ and Yoshiro OIKAWA³

¹ Graduate School of Hosei University, Tokyo 184-8584, Japan

² Technical University of Sofia, Sofia 1756, Bulgaria

³ Denshijiki Industry Co., Ltd. Tokyo 115-0051, Japan

Abstract— Eddy current testing (ECT) is one of the most representative nondestructive testing methods for metallic materials, parts, structures and so on.

This paper concerns with an improvement of sensibility of two types of ECT. One is conventional and the other is a separately sensing coil type ECT. Enhance the sensibility of the conventional ECT are mainly carried out by a classical analytical approach. On the other side, the other separately sensing coil type is fully exploited by a computational approach.

As a result, sensibility of the conventional ECT was enchanted to the 4th times higher than those of original one. Also a fully computer oriented designed type, i.e., the separately sensing coil type, displayed a remarkable sensibility with high liftoffs although it has directionality.

I. ENHANCEMENT OF THE CONVENTIONAL ECT SENSIBILITY

The first step of the conventional ECT is to select the optimum exciting frequency. Decision of ECT operation frequency is of paramount importance, because sensibility and searching depth of ECT are greatly depending on the operation frequency. We selected the natural parallel resonant frequency of the ECT sensor coil when facing with a wholesome part of target. When the ECT sensor coil meets with a defect of target, this resonance condition is essentially not satisfied. This makes it possible to maximize the deviation between the resonance and not resonance impedances.

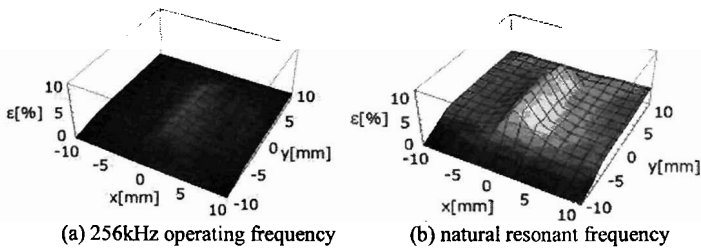


Fig.1 The results of defect searching

The second step of the conventional ECT is to increase a quality factor Q by changing the coil connection. The quality factor Q represents a sharpness of the resonant curve. Thereby the sensibility of the ECT is greatly depended on the quality factor Q . To increase this quality factor Q , we employed the resonant connection [1]. Due to these two steps, sensibility of the conventional ECT was enchanted to the 4th times higher than those of original one. Comparison of the line defect searching results in Fig.1(a) with those of Fig.1(b) reveals that the sensibility of resonant frequency operation (Fig.1(b)) is far superior than those of conventional ECT operating at 256KHz frequency (Fig.1(a)).

II. DEVELOPMENT OF A SEPARATELY SENSING COIL TYPE

Figure 2 shows our developed separately sensing coil type sensor that is composed of ∞ shape exciting coils and small searching coil wound around a ferrite bar. We named this sensor as " ∞ coil". This ∞ coil was innovated by a fully computational approach using the finite elements method.

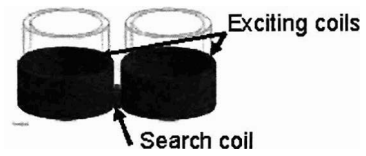


Fig.2 ∞ coil

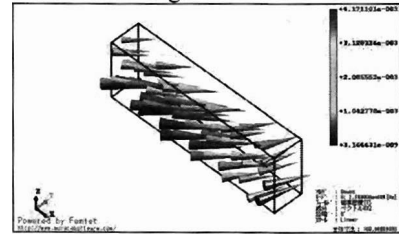


Fig.3 Magnetic flux density vector distribution when sensing a line defect.

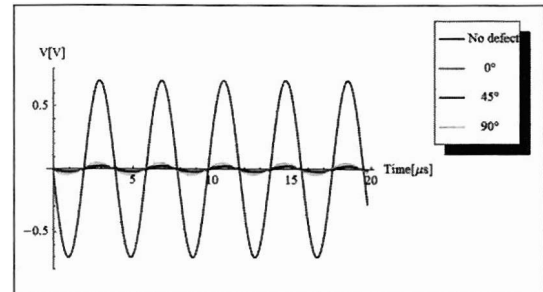


Fig.4 Measured voltage of the sensor coil.

Figures 3 and 4 show the computed magnetic flux density vectors distribution and the measured voltages of the search coil, respectively. A blue line in Fig.4 is the induced voltage when sensing a line defect. The other colored lines are the no defect or not directed angles. The most important key of the ∞ coil is that we set the sensor coil wound around a ferrite bar at the no or quite low magnetic fields space caused by the ∞ shape coils to detect only the magnetic fluxes due to the defect. This key location has been determined by an intensive computational approach using FEMTET by MURATA Software CO. LTD. Japan.

III. REFERENCES

- [1] Y.Midorikawa, S.Hayano and Y.Saito, A resonant phenomenon between adjacent series connected coils and its application to an als, Advanced Computational and Design Techniques in Applied Electromagnetic Systems, Vol.6, pp. 633-639, 1995.

第21回 MAGDA コンファレンス in 仙台

-電磁現象及び電磁力に関するコンファレンス-

講演論文集

会期： 2012年11月21日（水）～22日（木）

会場： 仙台市 戦災復興記念館

主催： 日本 AEM 学会

協賛： 日本機械学会，電気学会，日本磁気学会，日本シミュレーション学会，日本生体磁気学会，計測自動制御学会，システム制御情報学会，日本原子力学会，日本保全学会，日本非破壊検査協会，IEEE Magnetics Society (Japan Chapter)，プラズマ・核融合学会，日本ばね学会，ライフサポート学会，財団法人青葉工学振興会

新 ∞ 型渦電流センサの開発

Development of a new ∞ coil type eddy current sensor

菊地原弘基^{*1}、齊藤兆古^{*1}(正員)
大内学^{*2}、茂木秀夫^{*2}、及川芳朗^{*2}

Hiroki KIKUCHIHARA (Stu. Mem.), Yoshifuru SAITO (Mem.)
Manabu OUCHI(No Mem.), Hideo MOGI(No Mem.), Yoshiro OIKAWA(No Mem.)

Eddy current testing (ECT) is one of the most representative nondestructive testing methods for metallic materials, parts, structures and so on. Operating principle of ECT is based on the two major properties of magnetic field. One is that alternating magnetic field induces eddy current in all of the conducting materials. Thereby, an input impedance of the magnetic field source depends on the eddy current path. Second is that the magnetic field distribution depends not only on the exciting but also the reactive magnetic fields caused by the eddy currents in targets. Former and latter are the impedance sensing and magnetic flux sensing types, respectively.

This paper concerns with a development of a new magnetic flux sensing type sensor named " ∞ coil" whose exciting and sensing coils are composed of the ∞ shape exciting coil and finite length solenoid coil wound around ferrite bar, respectively. Development of this ∞ coil has been carried out by means of fully 2D and 3D finite elements computational scheme. According to the simulation results, we have worked out a proto type of ∞ coils. Practical experiments reflect on the validity of our key idea as well as computational results quite well.

Keywords: Eddy current testing, Nondestructive testing

1 緒言

現代の文明社会を支えるのは人類の叡智が創造した多くの文明の利器である。例えば、高速な移動手段を提供する高速鉄道、自動車、航空機、そして、電力生成・系統システム、照明システム、セキュリティシステムなど、いわゆる産業プロダクトから鉄橋、大型ビルや高速道路などの社会的インフラストラクチャまで広汎で多岐に渡る文明の利器が存在する。

これら文明の利器の多くは何らかの形で機械的構造を持ち、強度や形状維持のフレームが存在する。これらの多くは金属材料からなり、それぞれの産業プロダクトの機能を維持するため、機械的ストレスを受け続けている。産業プロダクトの中で、大量輸送に関わる大型バス、高速列車、大型旅客機のみならず、原子力発電所で代表される大規模エネルギー変換システムなどのプラントや社会的インフラストラクチャ設備では、機械的ストレスだけでなく熱応力、中性子による劣化などが発生する。当然ではあるが、これらの産業プロ

ダクトではフレームの健全性に高度な信頼性、安全性の確保が要求される。

金属の健全性を確保する手段として最も基幹的で重要な技術が、金属材料に対する非破壊検査技術である。金属の非破壊検査法として、渦電流探査法(Eddy Current Testing、以後 ECT と略記)、電気ポテンシャル法、超音波映像法および X 線断層撮影法のような様々な方法がある。この中で、ECT による方法は、検査対象と直接接触の必要がなく、比較的簡単な装置で高速な検査が可能である。このため、ECT は自動車の部品検査から橋梁の劣化検査など極めて多くの分野で広汎に使われている。これは、人類の創造する文明の利器の力学的強度維持は、大部分が導電性を有する金属材料からなるためであり、特に ECT は選択的に非接触で金属部分のみ検査可能である^{1,2)}。

本稿は ∞ 文字形状の励磁コイルと有限長ソレノイド型の検出コイルからなる渦電流センサ(以後 ∞ コイル)を提案する。

この ∞ コイルの動作は、励磁コイルの生成する磁束がゼロとなる領域へ検出コイルを配置し、被検査対象中の欠損に起因する磁束分布の乱れを検出コイルが感知する原理に基づく。

連絡先：菊地原 弘基、〒184-8584 小金井市梶野町 3-7-2、
法政大学大学院工学研究科電気工学専攻齊藤兆古研究室、
e-mail: hiroki.kikuchihara.6e@stu.hosei.ac.jp

^{*1}法政大学大学院工学研究科電気工学専攻

^{*2}電子磁気工業株式会社

2 ∞コイル

2.1 ECT センサの動作原理

ECTの動作原理は、大別して二方法がある。一方は交番磁界を被検査対象に照射することで被検査対象中に渦電流を発生させ、被検査対象中の欠損の有無による渦電流分布の相違を電源から見た入力インピーダンスの変化で感知する方法である。ここでは、このECT法をインピーダンス感知型と呼ぶ。このインピーダンス感知型 ECT の特徴は励磁コイルがセンサも兼ねる点にあり、構造が簡単で安価である。他方は励磁コイルの他に独立した検出コイルを備えた励磁・検出コイル分離型である。この励磁・検出コイル分離型は被検査対象中の欠損の有無に起因する渦電流分布の相違が喚起する磁束の変化を感知する検出コイルの配置に自由度を持つ。このため、励磁・検出コイル分離型は、インピーダンス感知型に比較して高感度とされているが、検出コイルの構造や設置場所などに多くの経験的習熟度を必要とする。本稿で述べる∞コイルの動作原理は励磁・検出コイル分離型に属する。

2.2 ∞コイルの動作原理

∞コイル開発の原点は、∞文字状に巻かれた二個の励磁コイルに通電すると、左右の励磁コイル下端ではN極とS極の磁極が形成される。N極とS極の磁極の間にはゼロ磁界領域が必ず存在する。このゼロ磁界領域へ磁性体コアに巻いた検出コイルを配置しても、被検査対象が存在しない、もしくは被検査対象に欠損が存在しない場合は励磁コイルが生成する磁界強度分布に対象性が保たれるから、ゼロ磁界領域も維持され検出コイルには電圧は誘起しない。

換言すれば、N極とS極間には必ずゼロ磁界領域が存在する。励磁コイルが生成するN極とS極の磁界強度分布が対象である限り、励磁コイル間の磁界がゼロ領域は維持される。しかし、被検査対象に欠損があれば、欠損に起因する渦電流分布の非対称性に起因する磁界は検出コイルへ鎖交する。結果として検出コイルに電圧が誘起し欠損が探知される。

実際は、磁界がゼロ領域は限られた微小範囲であるため、検出コイルの軸は磁界がゼロ領域を取り囲むようにゼロ領域へ平行に配置する。すなわち、∞文字状の励磁コイル軸へ直交する方向へ検出コイルの軸を配置し、励磁コイルと検出コイル間の相互インダクタンスをゼロにする。両者に相互結合が起こるのは検査対

象の欠損を通した場合のみとする。これが回路的な観点から見た∞コイルの動作原理である。

2.3 ∞コイルの解析モデル

∞コイルは三次元有限要素法によるシミュレーションを用いての開発した³⁾。

Fig.1 は∞文字に対応する二個の隣接する励磁コイルを示し、Fig.2(a)はこれら二個の励磁コイルに互いに逆位相の電流を流した場合の磁束密度強度分布を示す。コイル内の磁束密度強度に比較して極めて小さい磁束密度強度を持つ領域が二個の励磁コイル間に存在する。Fig.2(b)は二個の励磁コイル間にフェライト棒に巻いた検出コイルを挿入したシミュレーション結果である。検出コイルを磁束密度の強度が極めて小さい領域に配置したため、励磁コイルが生成する磁束密度強度分布はFig.2(a)と変わらない。

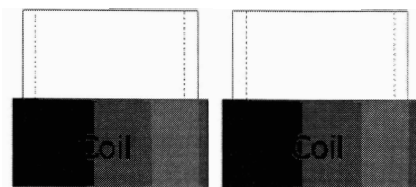
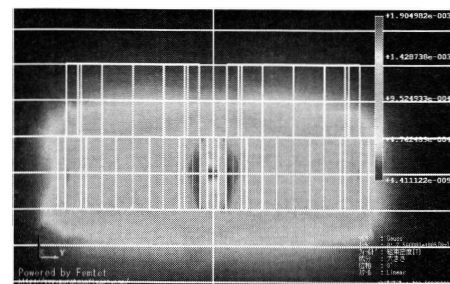
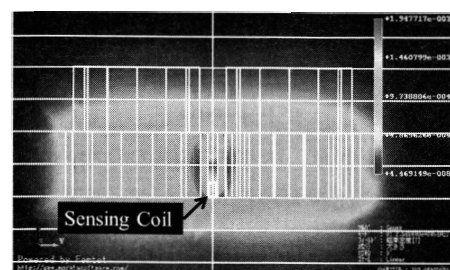


Fig.1 Two exciting coils.



(a) Without ferrite bar



(b) With ferrite bar

Fig. 2 Magnetic fields intensity distribution.

Figs.2(a)と 2(b)が殆んど同じ磁束密度強度分布となることは、極めて小さい磁束密度強度を持つ領域に磁

性体が存在しても、全体の磁束密度強度分布に殆んど影響しないことを意味する。換言すれば、検出コイルを棒状磁性体へ巻いて構成でき、仮に検出コイルが存在する部分が非ゼロ磁界になった場合、磁界は検出コイルへ集中することを意味する。

2.4 シミュレーション

Fig.3 に示す ∞ コイルの動作原理を検証するために三次元の有限要素法によるシミュレーションを行う。

Table 1 に励磁コイルと検出コイルの諸定数を示す。 ∞ コイルが厚さ 1mm の被検査対象とする銅板上に配置され、欠損が無い場合、検出コイルに対し欠損が 0 度、90 度、45 度の場合に関してシミュレーションを行う。

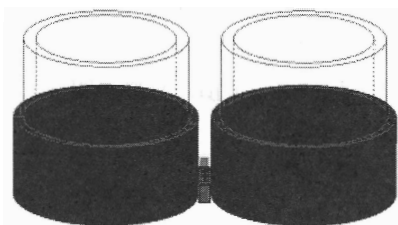


Fig.3 3D simulation model of the ∞ coil

Table 1 various constants used in the 3D FEM simulation.

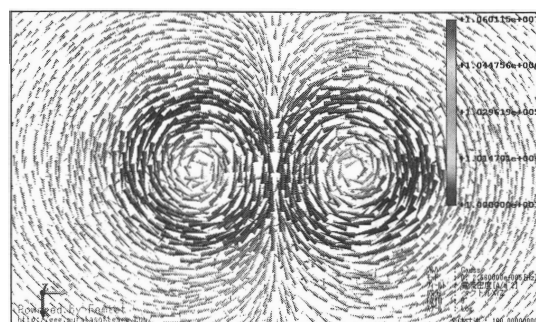
Coil outer diameter	22.4mm
Coil inner diameter	20mm
Coil length	10mm
Number of turn	75
Input current(peak)	250mA
	256kHz
Sensing coil	
Coil outer diameter	1.4mm×2.4mm
Coil inner diameter	1mm×2mm
Coil length	6mm
Number of turn	100
Axis core	JFEferrite_MB1H_23°C

Figs.4、5 はそれぞれ被検査対象とする銅板上に流れる渦電流と検出コイルのフェライトコア内の磁束密度ベクトル分布を示している。

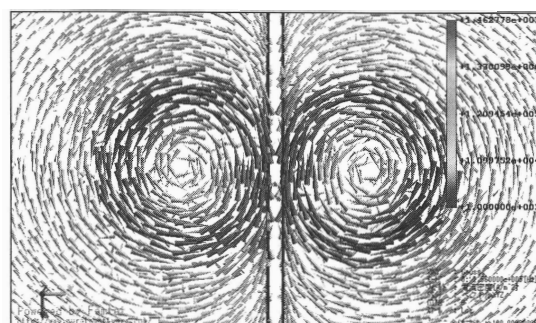
被検査対象とする銅板中に欠損が存在しない場合、Fig.4(a)に示す渦電流分布となる。渦電流によって生じる磁束密度ベクトルは検出コイルの面に対し平行方向のみであるため Fig.5(a)に示す方向となり、検出コイルに誘起電圧は発生しない。

Fig.4(b)は被検査対象とする銅板中に存在する 2mm 幅の直線状欠損を検出コイルに対し 0 度に配置された場合の渦電流分布である。渦電流は欠損に沿う方向に

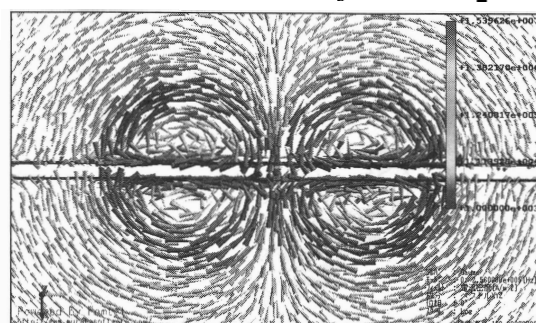
流れるが、渦電流が流れる方向は欠損が無い場合と同じであるためフェライトコア内の磁束密度ベクトルは Fig.5(b)に示す方向となる。このため、検出コイルの面に垂直方向磁束密度ベクトルが存在せず検出コイルに誘起電圧は発生しない。すなわち、欠損が検知できない。



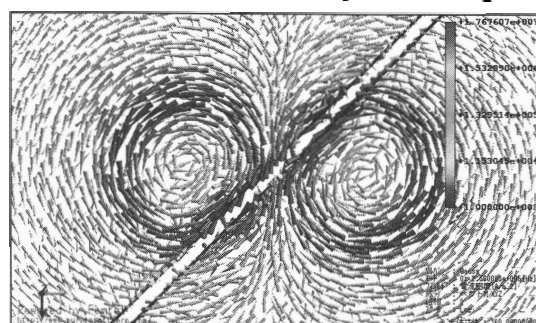
(a) No defect



(b) 0 degree defect to the two adjacent exciting coils

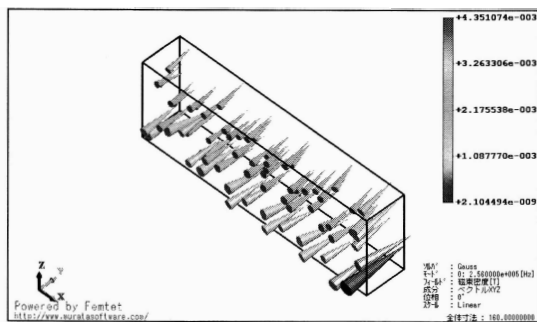


(c) 90 degree defect to the two adjacent exciting coils

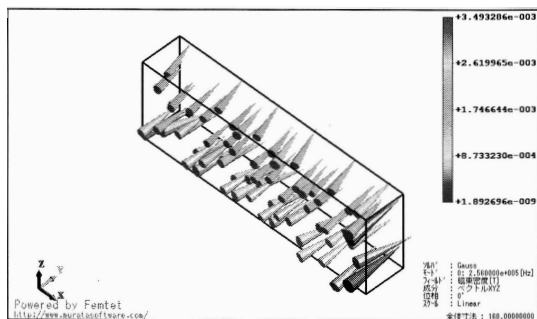


(d) 45 degree defect to the two adjacent exciting coils

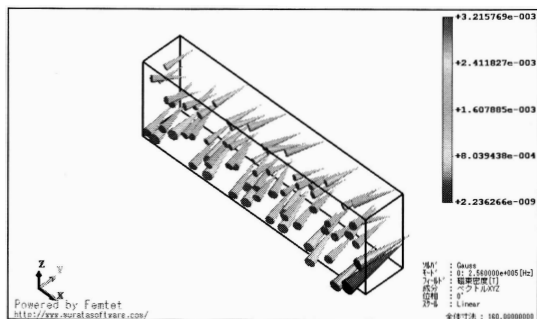
Fig.4 Eddy currents in a plane metallic target.



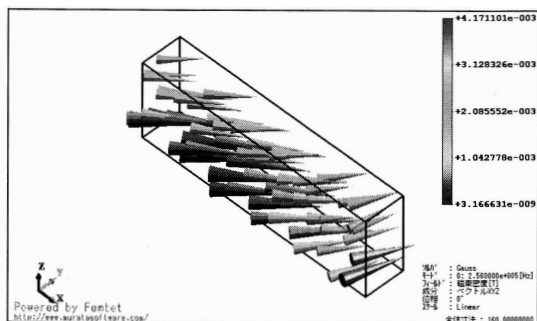
(a) No defect



(b) 0 degree defect to the two adjacent exciting coils



(c) 90 degree defect to the two adjacent exciting coils



(d) 45 degree defect to the two adjacent exciting coils

Fig.5 Magnetic flux density vector distributions in the ferrite bar

Fig.4(c)に被検査対象とする銅版中に存在する 2mm 幅の直線状欠損を検出コイルに対し 90 度に配置された場合の渦電流分布を示す。銅板中の渦電流は欠損によって妨げられ検出コイル面に垂直な方向の磁束密度ベクトルを生成する方向に流れる。しかし、二個の励

磁コイルそれぞれに起因する渦電流は互いに逆方向であるため、両者の生成する磁束密度ベクトルは欠損の両端で互いに打ち消し合い、フェライトコア内の磁束密度ベクトルは Fig.5(c)に示すようにフェライトの断面方向へ平行となり、検出コイルに誘起電圧は発生せず、欠損を検知できない。

Fig.4(d)は被検査対象とする銅版中に存在する 2mm 幅の直線状欠損が検出コイルに対し 45 度に配置された場合の渦電流分布を示す。渦電流は欠損に沿って流れ、Fig.5(d)に示すように検出コイル断面に垂直成分を含む磁束密度ベクトルが生ずる。この結果、検出コイルに誘起電圧が発生し欠損が検知される。

Figs.5(a)-(d)における検出コイルの誘起電圧を Fig.6 に示す。Fig.6 は被検査対象とする銅版中に存在する 2mm 幅の直線状欠損が検出コイルに対し 45 度の場合、高い誘起電圧が発生し欠損の有無が明確に識別されることを示す。

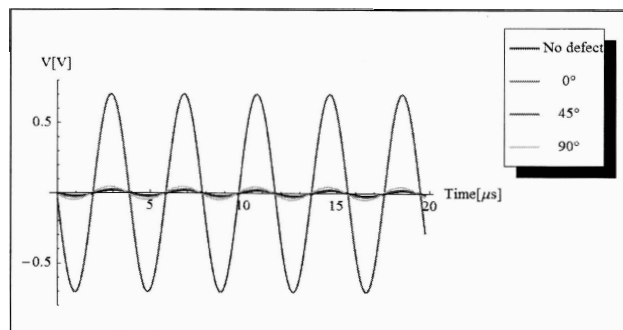


Fig.6 Induced voltages in the sensor coil

3 実験

3.1 試作∞コイル

Table 2 Various constants of the prototype ∞ coil.

Conductor length	4.7m
Diameter of conductor	0.4mm
Coil outer diameter	23mm
Coil inner diameter	20mm
Coil length	10mm
Number of turn	75
Number of coil layers	3
Number of coils	2
Input current(peak)	250mA
	256kHz
Conductor length	60cm
Diameter of conductor	0.1mm
Axis core	Ferrite bar (MnZn)
Coil outer diameter	2.4mm×2.4mm
Coil inner diameter	1.4mm×1.4mm
Coil length	6mm
Number of turn	100
Number of coil layers	2
Number of coils	1

被検査材料として厚さ 1mm、長さ 10cm、幅 10cm の銅板二枚を使用する。一方は欠損が無く、他方は幅が 2mm 長さ 5cm の直線状貫通欠損を持つ。

Table 2 は ∞ コイル試作に使用した励磁コイルと検出コイルの諸定数を示す。

Fig.7 に示すように試作 ∞ コイルは二個の励磁コイルと一個の検出コイルからなる。この ∞ コイルの諸定数は三次元有限要素法によるシミュレーションで使用した Fig.3 のそれらと同一である。

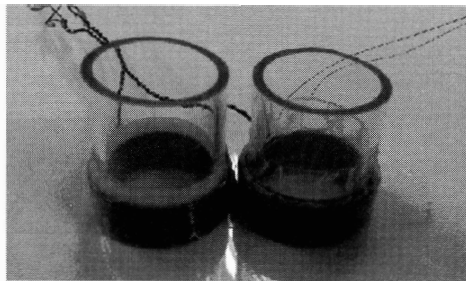


Fig.7 Picture of the prototype ∞ coil.

3.2 実験結果

Fig.7 に示す ∞ コイルを被検査対象上に配置し、欠損が無い場合、検出コイルに対し欠損が 0 度、45 度、90 度の場合に対する検出コイルに誘起する電圧を測定する。

Fig.8 は検出コイルに誘起する電圧の実測値である。Fig.8 からシミュレーション結果と同様に欠損が検出コイルに対し 45 度の場合に高い誘起電圧が発生することが判る。また、Fig.6 のシミュレーション結果と比較して実測値は約半分程度の振幅となるが、欠損に対する検出電圧の傾向は一致する。

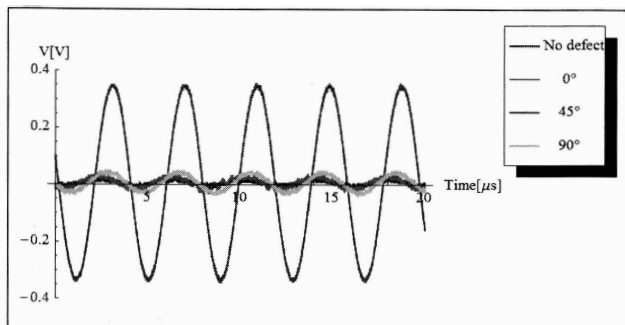


Fig.8 Measured voltages of the practical sensing coil.

以上の結果から、 ∞ コイルの動作原理が検証され、提案した ∞ コイルは欠損検知感度に指向性を有するが、比較的高い S/N 比を持つことが判明した。これは、 ∞

文字状に巻かれた励磁コイルの作る磁束密度分布は必ず二個の励磁コイル間にゼロ磁束密度領域が存在することに着目し、ゼロ磁束密度領域へ検出コイル配置した着想を反映した結果と考えられる。

4 結論

本稿は「 ∞ コイル」と称する新しい ECT センサを提案し、その着想の妥当性を有限要素法によるシミュレーションと実際の実験結果で検証した。

∞ コイルは、人間の着想を有限要素法によるシミュレーションで可視化し、励磁コイル間のゼロ磁界領域の存在を確認し、さらにゼロ磁界領域に磁性体を配置した場合の磁界分布を吟味して開発された。

∞ コイルの基幹的着想は、励磁コイルが作る磁束密度強度分布が変化しない限り励磁コイル間に存在するゼロ磁界領域も維持される。しかし、被検査対象中の渦電流分布が欠損によって乱され、全体の磁束密度強度分布が変化した場合、ゼロ磁界領域が非ゼロ磁界領域となる現象を利用した点に尽きる。この基幹的着想はシミュレーションと実験で裏付けられた。

本稿の三次元有限要素法解析はムラタソフトウェア株式会社の「Femtet」で行われた。

参考文献

- [1] I.Marinova, S.Hayano and Y.Saito, Ployphase eddy current testing, Journal of Applied Physics, Vol. 75, No.10, pp. 5904-5906, 1994.
- [2] N.Burais and A.Nicolas, Electromagnetic field analysis in remote field eddy current testing systems, IEEE Transactions on Magnetics, Vol.25, No.4, pp.3010-3012, 1989.
- [3] S.McFee and J.P.Webb, Automatic mesh generation for h-p adaptation, IEEE Transactions on Magnetics, Vol.29, No.2, pp.1894-1897, 1993.

最適化手法に基づく非接触給電用変圧器の開発

Development of Contactless Transformers for Contactless Power Suppliers Based on Optimization Methodology

大橋 竜也^{*1}(学生員)、齊藤兆古^{*1}(正員)

Tatsuya OHASHI (Stu. Mem.), Yoshifuru SAITO (Mem.)

Contactless power supplier is composed of a transformer having the distinct primary and secondary cores separated by air gap. Because of the electromagnetic compatibility problem, it is essential to keep the leakage magnetic fields around the contactless power supplier as possible as low.

Previously we have clarified that the wavelets multi-resolution analysis to the magnetic field distributions around contactless transformer leads to obtain one of the reasonable core shapes by observing the wavelets spectra of measured magnetic field vector distributions. Furthermore, it has been revealed that a tested trial transformer gives nearly 80 percent power transmission efficiency even though the primary and secondary coils cores are separated by 10mm air gap.

This paper is one of the success research solutions to overcome the specific absorption rate (SAR) problem based on the finite elements and optimization methodologies. Namely, a contactless flat shaped transformer whose primal and secondary ferrite cores are separated has been successfully optimized by combining the finite elements with linear programming optimization approaches.

Keywords: contactless transformer, magnetic field visualization, SAR, optimization.

1 緒言

半導体技術の発展は、電気・電子機器の小型軽量化のみならず、インテリジェント化を可能とし、爆発的な電気・電子機器の普及をもたらした。その結果、高周波で駆動される電気・電子機器は生産設備のみならず家電機器まで広汎に普及し、家庭、事務所、工場、その他あらゆる場所でパソコン、ファックス、携帯電話、空調設備、照明機器等の多くの電気・電子機器が設置され、必要不可欠な文明の利器として活用されている。それらの電気・電子機器が空間を占める密度は、従来想定不可能な密度である。この意味で、現代の人工空間はあらゆる周波数の電磁界で満たされている。これは SAR (Specific Absorption Rate) 問題を喚起することに他ならない。

この過酷な電磁環境中でも、電気・電子機器は誤作動をすることなく円滑にそれらの機能を発揮しなければ

ば人類の文明生活が維持できない。換言すれば、あらゆる周波数の電磁界で満たされた空間の中で人類は生活を強いられている状況である。電気・電子機器に対してだけでなく人類に対しても可能な限り、電磁界が分布しない自然な空間が望ましいことは言うまでもない。

生活環境中における電磁環境 (ElectroMagnetic Compatibility) 問題の解決策の一つは、低 SAR レベルの非接触給電システム開発にある。この非接触給電システムの最基幹部品が一次・二次コア分離型変圧器である。

本稿は、エアギャップによって分離された一次・二次分離型変圧器開発に関するものである。すなわち、本稿では、先行研究で明らかにされたスプーン皿形状の外鉄型磁性コアを用いた一次・二次コア分離型変圧器の設計定数を有限要素法で求め、さらに、有限要素法で求められた設計定数を用いて二次共振型変圧器の動作周波数と共振用キャパシタンスを最適化手法によって決定する¹⁻³⁾。その結果、1cm のエアギャップが存在しても一次・二次電力伝送効率 80% 近くが得られるこ

連絡先：大橋 竜也、〒184-8584 小金井市梶野町 3-7-2, 法政大学大学院工学研究科電気工学専攻齊藤兆古研究室, e-mail: tatsuya.ohashi.6z@stu.hosei.ac.jp

^{*1} 法政大学大学院工学研究科電気工学専攻

とが判明し、この結果は実験によって検証された。

2 一次・二次コア分離型変圧器の基礎特性

2.1 コア形状

非接触給電システムではエアギャップを介して電力電送を行う。このため、一次・二次コア分離型変圧器は最も重要な基幹部品である。

一般に変圧器のコア材である磁性体は重量が重いいため、コア材の量を可能な限り削減することが望まれる。これは通常動作周波数の高周波化でなされる。高周波特性のよい磁性材料はフェライトである。

一次・二次コア分離型変圧器では、電力伝送がエアギャップを介して行われるため、変圧器周辺の漏れ磁界が最小であることが必須である。離散値系ウェーブレット変換の多重解像度解析を用いた変圧器周辺の磁界ベクトル分布解析から、磁性体コアの形状は外鉄型的一种であるスプー皿型が最適であることが判明している^{1,2)}。

この結果を踏まえ、各種のスプー皿形状のフェライトコア形状と一次・二次巻線形式に関して有限要素法に拠る数値シミュレーションを行った。その結果、既存のスプー皿形状のフェライトコアの中から Fig.1 に示す同一形状のスプー皿型フェライトコアを一次・二次コア分離型変圧器として採用した。

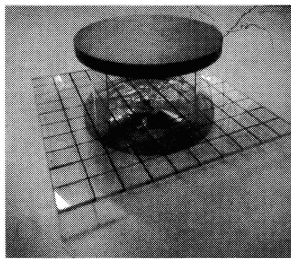


Fig.1 A tested flat shape ferrite core transformer.

2.2 磁界ベクトル分布

Fig.1 に示すスプー皿型フェライトコアを有する変圧器で、二次側へ 1Ω の負荷抵抗と共振用キャパシタンスを接続し、二次側共振状態下の磁界ベクトル分布の測定例を Fig.2 に示す。Fig.2 は一次・二次コア間の磁界ベクトルの xyz 三成分を、コアに平行な x-y 平面とコア面に垂直な高さ方向を z 方向とした測定結果である。Fig.2 から、主要な磁束は一次・二次コア中心部に集中し、コア端部から漏れる磁束密度ベクトルが殆んど無いことが判る。

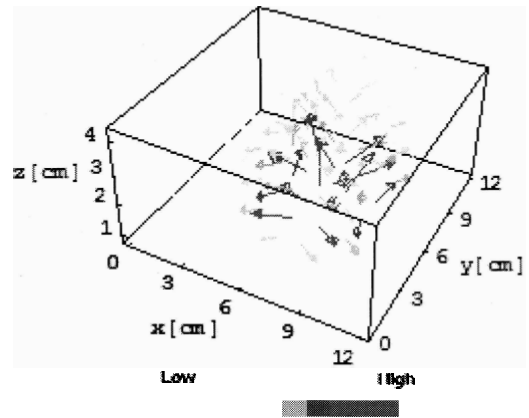


Fig.2 One of the magnetic field vector distributions of the tested transformer under the 1Ω pure resistive load and secondary resonant conditions.

2.3 結合係数

一次・二次コイル間の漏洩磁束の過多を表す指標である結合係数 κ は変圧器の最も重要な性能指標の一つである。すなわち、結合係数 κ が大きいことは変圧器周辺の漏洩磁束が小さいことを意味する。

変圧器の一次・二次コイルを Fig.3 に示す回路モデルで考える。Fig.3 の端子 a,b,c,d を Fig.4 に示すように結線し、インダクタンスを測定することで式(1)から結合係数 κ が求まる。

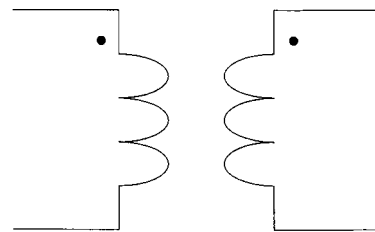


Fig.3 Circuit model of transformer.

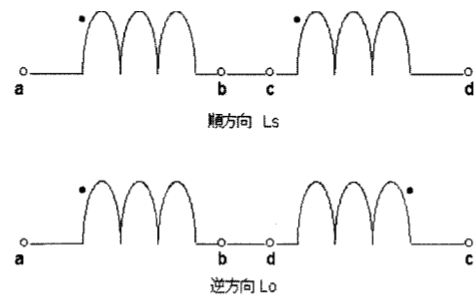


Fig.4 Series connection of the primary and secondary inductances.

$$\begin{aligned}
 L_s &= L_1 + L_2 + 2M, \\
 L_o &= L_1 + L_2 - 2M, \\
 M &= \frac{L_s - L_o}{4} \\
 \therefore k &= \frac{M}{\sqrt{L_1 L_2}}
 \end{aligned}
 \tag{1}$$

Table 1 にスープ皿型フェライトコアを使用した変圧器の結合係数 κ を示す。Table 1 の結果から、スープ皿型フェライトコアを使用した変圧器は 5mm 程度のエアギャップが存在しても結合係数が 80% を越える十分な磁気結合を維持することがわかる。

Table 1 Coupling factor of the tested transformer employing soup plate like shape cores measured at 30kHz.

Gap[mm]	0	1	3	5	7	10
$L_1[\mu\text{H}]$	578.6	348.2	231.1	181.6	169.9	133.9
$L_2[\mu\text{H}]$	572.7	348.1	229.4	181.0	168.3	133.3
$L_s[\mu\text{H}]$	2297.4	1358.2	881.8	669.4	617.6	450.8
$L_o[\mu\text{H}]$	16.9	26.1	41.4	56.0	61.1	84.3
κ	0.99	0.96	0.91	0.84	0.82	0.69

2.4 一次・二次電力伝送効率

一次側から二次側へ伝送される電力の伝送効率もまた変圧器の重要な性能指標の一つである。本稿では、Fig.5 に示すように二次側にコンデンサを接続し、二次側漏れインダクタンスとコンデンサ間に共振回路を形成し伝送効率の改善を図る³⁾。

一次・二次コア間のギャップを 10mm、二次側に純抵抗負荷 1Ω、共振用コンデンサ 40μF、動作周波数 30kHz に設定し、式(2)より算出した伝送効率の実験値は約 80% となり、一次・二次コア間のギャップが 10mm である一次・二次コア分離型変圧器の電力伝送効率としては良好と言える。

また、後述する線形計画法による最適化理論による結果から、この比較的良好な伝送効率を維持するコンデンサと周波数の選択幅は十分に広い。

$$\varepsilon = \frac{\text{Secondary output power}}{\text{Primary input power}} \times 100 [\%]
 \tag{2}$$

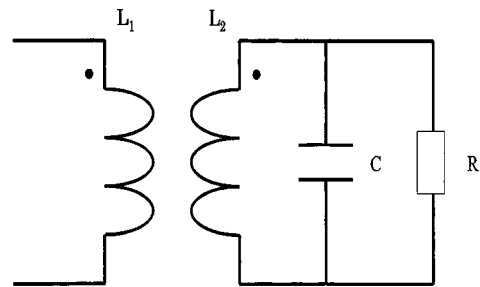


Fig. 5 Circuit diagram model of a secondary resonant type transformer.

3 有限要素シミュレーションと最適化手法

3.1 有限要素シミュレーション

有限個のスープ皿型フェライトコアの中から、漏洩磁束を最小化するフェライトコア形状と一次・二次巻線形式を有限要素法に拠る数値シミュレーションで選択した。Fig.6 にシミュレーションに用いたモデルを示す。なお、数値シミュレーションは、汎用有限要素法パッケージ Femtet (MURATA ソフトウェア)で行った。



Fig.6 Simulation model of the transformer employing the soup plate like ferrite cores.

Fig.7 は一次・二次コア間のギャップ長に対するインダクタンス値を実験値と共に示す。Fig.7 の結果から、シミュレーションと実験、いずれの場合もインダクタンスはギャップ長に反比例して減少する傾向を示し、両者の値が殆んど一致することが判る。

したがって、Fig.6 に示したシミュレーションモデルの妥当性が検証された。

Fig.8 は、シミュレーションによる一次・二次コア分離型変圧器の磁束密度ベクトル分布の一例を示す。

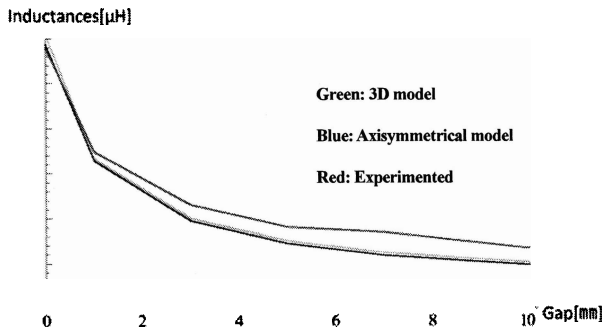


Fig.7 The computed self-inductances versus air-gap length.

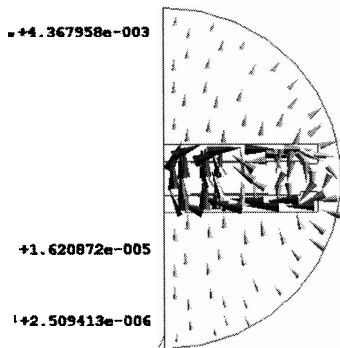


Fig.8 One of the simulated magnetic field vectors distributions of the transformer. Unit of color bar is Tesla.

3.2 共振用コンデンサと動作周波数の最適化

式(2)で与えられる一側から二次側へ伝送される電力の伝送効率 ε は、一次コイルの抵抗 r_1 、自己インダクタンス L_1 、一次・二次間の相互インダクタンス M 、二次コイルの抵抗 r_2 、二次負荷抵抗 r 、二次共振用コンデンサ C 、さらに動作周波数 f の関数であるから、

$$\varepsilon = f(r_1, r_2, r, L_1, L_2, M, C, f) \quad (3)$$

で表される。

一次コイルの抵抗 r_1 、自己インダクタンス L_1 、一次・二次間の相互インダクタンス M 、二次コイルの抵抗 r_2 は一次・二次コアや巻線の幾何学的寸法と媒質のパラメタで決まる。さらに、二次負荷抵抗 r は 1Ω とする。このため、式(3)の伝送効率 ε が最大となるコンデンサ C と動作周波数 f を線形計画法 (Linear Programming) で求める。

すなわち、

$$\varepsilon \rightarrow \max \quad (4)$$

となるコンデンサ容量 C と動作周波数 f を求める。Fig.9 が結果である。

Fig.9 の結果は比較的大きい 10mm のエアギャップを有する場合の伝送効率であり、80%以上の効率を得

るコンデンサ容量と動作周波数の組み合わせが複数存在することを示す。この結果は 2.4 節で実験的に得られた結果を裏付けている。

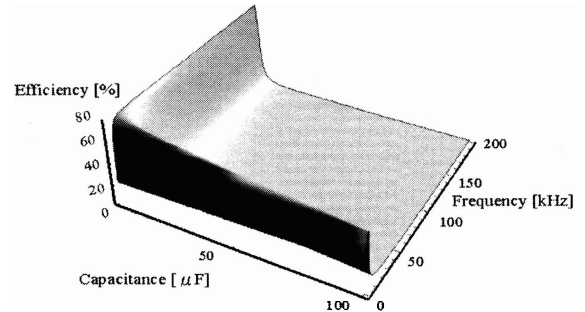


Fig.9 Power transmission rate by the linear programming optimization.

以上の結果から、有限要素法による磁界分布解析や線形計画法による伝送効率の最適化など、現代の計算機を用いた解析手法を駆使して非接触給電用一次・二次分離型変圧器設計の一手法を確立した。

4 結言

低 SAR を実現する非接触給電用一次・二次分離型変圧器を設計するために、有限要素法を用いて一次・二次磁性体コア形状や巻線形式を選定し、変圧器の回路定数、抵抗、インダクタンスを算出した。さらに、それらの回路定数を用いて、特定の負荷時における二次共振型変圧器の最適なコンデンサ容量と動作周波数を線形計画法で決定し、非接触給電用一次・二次分離型変圧器設計の一手法を確立した。

参考文献

- [1] S.Takada, Y.Saito and K.Horii, Visualization of the magnetic field vectors around the contact-less power suppliers, Japan Society of Visualization, Proceedings of the Visualization Symposium in 2000, Paper No. P01-001.
- [2] S.Matsuyama, Y.Oguchi, Y.Saito, T.L.Kunii, Handling Technique of the Dynamic Color Computer Graphics by the Wavelets transform, Japan Society of Visualization, Proceedings of the Visualization Symposium in 1999, Paper No. 206.
- [3] J.L. Harrison, A new resonance transformer, Electron Devices, IEEE Transactions on Issue Date: Oct 1979 Vol.26 Issue: 10, pp. 1545 - 1.